ORIGINAL PAPER

Mineral chemistry and Petrology of the Andarian volcanic rocks: insight to the Ahar-Arasbaran magmatic zone, Northwestern Iran

Elahe Namnabat[1] · Mansour Ghorbani[1] · Kazuo Nakashima[2] · Seyed Hassan Tabatabaei[3] · Neda Tavakoli[4]

Abstract

The Neogene Andarian volcanic rocks, a part of the Ahar-Arasbaran magmatic zone, are situated in the northwest of Iran. These units are composed of a series of intermediate to acidic volcanic rocks including basaltic andesite, hornblende andesite, andesite, dacite, and rhyodacite. The basaltic andesite and hornblende andesite are mainly comprised of K-feldspar (Or_{10-63}), plagioclase (An_{5-37}), calcic amphibole, clinopyroxene (En_{45-64} Wo_{29-54} Fs_{0-20}), and biotite (Mg#: 0.70–0.82). The compositions of biotite, clinopyroxene, and amphibole as well as whole rock chemistry of the Andarian volcanic rocks show calc-alkaline signatures. The amphibole-plagioclase thermometer and Al-in-hornblende barometer data yielded crystallization temperatures of 707–899°C and pressures of 0.5 to 2.9 kbar. The negative Nb, Ta, and Ti anomalies and large ion lithophile element (LILE; Rb, Ba, and Sr) enrichments relative to primitive mantle indicate a subduction setting. Furthermore, the chondrite-normalized rare earth element (REE) patterns show an LREE enrichment with no clear Eu anomaly. Amphibole and clinopyroxene compositions indicate crystallization under strongly oxidizing conditions.

Keywords Andarian · Ahar-Arasbaran magmatic zone · Calc-alkaline · Andesite

Responsible Editor: Domenico M. Doronzo

✉ Elahe Namnabat
elahe.n65@gmail.com

Mansour Ghorbani
m_ghorbani@hotmail.com

Kazuo Nakashima
nakashi@sci.kj.yamagata-u.ac.jp

Seyed Hassan Tabatabaei
tabatabaei@cc.iut.ac.ir

Neda Tavakoli
neda.tavakoli87@gmail.com

[1] Faculty of Earth Sciences, Shahid Beheshti University, Tehran, Iran

[2] Department of Earth and Environmental Sciences, Yamagata University, Yamagata, Japan

[3] Department of Mining Engineering, Isfahan University of Technology, Isfahan, Iran

[4] Faculty of Natural Resources and Earth Sciences, Shahrekord University, Shahrekord, Iran

Introduction

The Ahar-Arasbaran magmatic zone (AAMZ) located in the southern part of the Lesser Caucasus (Fig. 1) with WNW–ESE trending. The position of the Lesser Caucasus provides a unique opportunity to understand the lateral connection of the central and western Tethyan metallogenic belt (Richards 2015). The AAMZ shows a complex geology and tectonic setting due to its proximity to the Arabia-Eurasian collision (Avagyan et al. 2018; Matossian et al. 2020). Lithospheric variations and faults are the main parameters affecting the tectonic evolution of the Lesser Caucasus (Avagyan et al. 2005). The AAMZ is situated in the hinterland of the Arabia–Eurasia collision zone and the edge of the Alpine-Himalayan tectonic belt (Dilek et al. 2010; Aghazadeh et al. 2012). This zone is 1500 km long and 150 to 200 km wide (more than 23000-km^2 area) and is exposed in the northwestern part of Iran and extends to Azerbaijan and Armenia (Castro et al. 2013; Hassanpour et al. 2015; Pazand and Hezarkhani 2018).

The AAMZ is limited by the Aras, Talesh, and Tabriz faults (Castro et al. 2013) and known as a high potential prospect for copper, gold, and molybdenum mineralization (Akbarpur 2007; Jamali et al. 2010; Moritz et al. 2011;

Fig. 1 Simplified structural map of Iran (modified from Stocklin 1968; Hassanpour 2017)
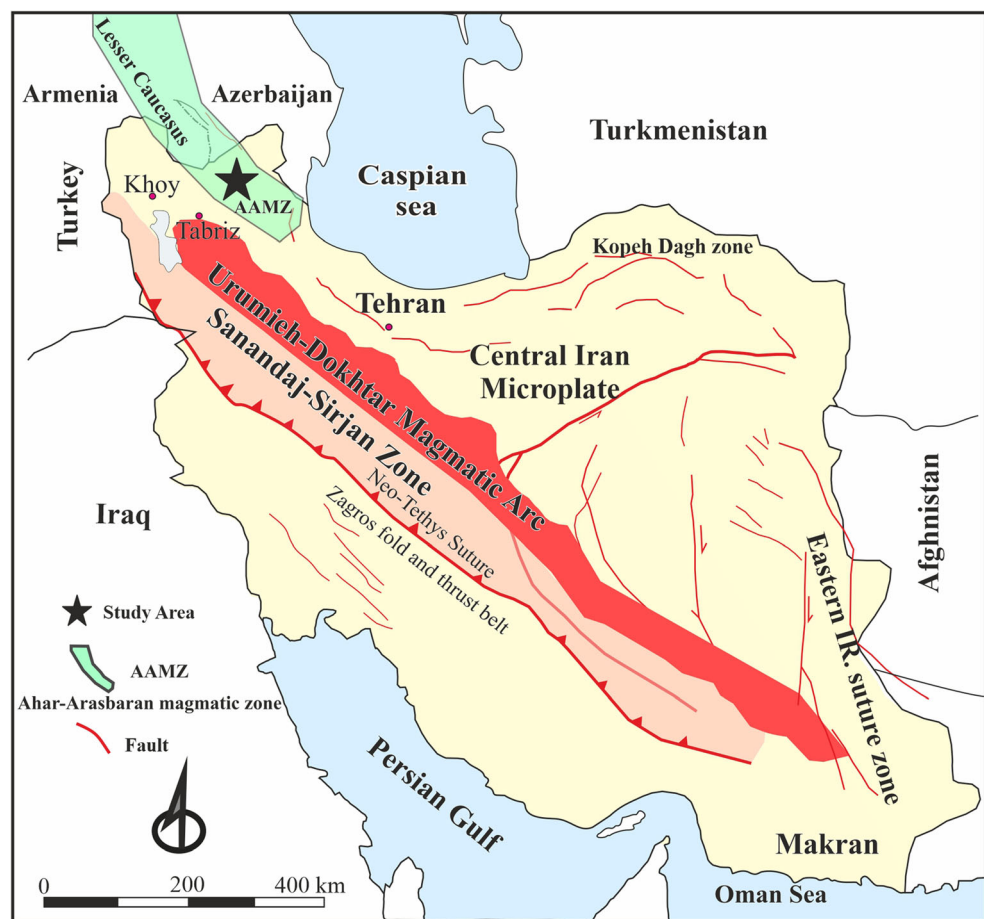
Maghsoudi et al. 2014; Hassanpour et al. 2015; Richards and Sholeh 2016; Moritz et al. 2016; Simmonds et al. 2017; Rabiee et al. 2019). The AAMZ shows extensive magmatic activity from the Upper Cretaceous to Quaternary with few time gaps (Ghorbani 2013; Simmonds et al. 2017). The following five magmatic episodes are recognized in the AAMZ:

1) Middle Cretaceous to Paleocene magmatic activity, where high-thickness (up to 1000 meters thick) Middle Cretaceous volcanic sequences underlay Late Cretaceous limestone units. These units consist of high-K calc-alkaline, calc-alkaline and tholeiitic lava flows, and pyroclastic rocks (Vincent et al. 2005; Aghazadeh et al. 2010; Hassanpour 2010; Jamali and Mehrabi 2015; Soltanmohammadi et al. 2018).

2) Eocene volcanic phase, which marks the peak of the volcanic activity in the AAMZ (with a climax in the Middle Eocene). The volcanic rocks of this sequence are mainly intermediate to acidic in composition while pyroclastic rocks (mainly tuff) of this sequence are predominantly acidic. This stage of volcanism is accompanied by widespread hydrothermal alteration and mineralization. This magmatic episode mostly includes alkaline and shoshonitic volcanic rocks, which are overlain by Late Eocene flysch-type sediments and/or Late Miocene volcanic and sedimentary units (Dilek et al. 2010).

3) Late Eocene to Early Oligocene magmatic phase, is generally composed of small and large intrusions in the AAMZ area, generated various and wide hydrothermal alterations (Jamali et al. 2010; Hassanpour 2013; Ghorbani 2013). These intrusive bodies with NW-SE trend, which cut Middle Eocene volcanic rocks, comprise nepheline syenite, monzonite, granodiorite, quartz-diorite, and granite (Jamali et al. 2010). Locally, part of the intrusive rocks is covered by Oligo-Miocene red beds (Upper Red Formation) implying that they may Middle Oligocene or older in age.

4) The Middle Oligocene-Pliocene magmatic stage mainly consists of acidic volcanic domes and sub-volcanic rocks (Ghorbani 2013). According to Hassanpour et al. (2015), the development of the main porphyry Cu–Mo mineralization in the AAMZ is related to this phase (Early Miocene). Comparing with the second episode, this magmatic phase shows widely variable lithological characteristics.

5) The Quaternary alkaline basaltic and andesitic lavas (the last volcanic stage in the AAMZ) have been linked to the collision of the Afro-Arabian and Eurasian plates

(Kheirkhah et al. 2009; Dabiri et al. 2011). The rock composition indicates a subduction setting with a distinct enrichment in lithophile elements and a high La/Nb ratio (Kheirkhah et al. 2009). The volcanic rocks studied here are representative of the fourth magmatic episode. No detailed studies have been conducted on the Neogene volcanic rocks in the Andarian area. The main aim of this paper is to determine the geochemistry, petrogenesis, and nature of the magma source, as well as the tectonic setting characterized by the mineral composition and whole rock chemistry data for the Andarian volcanic rocks.

Geological setting

The Andarian region is situated in the East Azerbaijan province (NW Iran), about 51 km north of Tabriz city (Fig. 1). Andarian area exhibits a complex geology with a combination of intrusive igneous rocks, altered and mineralized rocks, low-metamorphic rocks, and volcanic rocks. Upper Cretaceous-Paleocene sedimentary rocks are exposed on the west of the Andarian village (Ghorbani 2019; Fig. 2). This sequence is generally composed of flysch deposits, thick sequences of limestones and marls, alternating with sandstones and silt-stones. Sedimentary units, volcanic rocks, pyroclastic, and volcano-sedimentary rocks are the main constituent of Eocene outcrops in this area (Fig. 2). The Miocene Mivehrood pluton (Hassanpour et al. 2015; Fig. 2) comprises granodiorite, diorite, quartz-monzodiorite, and quartz-

monzonite with porphyritic to granular textures (Ferdowsi et al. 2015; Alirezaei et al. 2015). Contact aureoles (skarn and hornfels) formed by penetration of the pluton (stock) associated dykes and sills into the Upper Cretaceous sediments. Alirezaei et al. (2015) found that these skarns occur as a ring around the intrusive body. Hornfelses (with about 100 m thick) occurred in the contact with the skarns. The hornfelses show a dark color in hand specimens and consist of recrystallized feldspars and quartz, dolomite, calcite, micas, epidote, and wollastonite (Alirezaei et al. 2015). The Pliocene rocks (evidently Pliocene) consist of three units, a volcanogenic conglomerate, acidic to intermediate volcanic rocks (present work) and lava flows. These volcanic rocks overlay the Oligo-Miocene sedimentary beds (Qom Formation) near the Andarian village (Fig. 3a). Thus, field evidence suggests that the age of these volcanic rocks is late Miocene and younger (they are also known as post-Miocene volcanic rocks). In other parts of the AAMZ, the volcanic domes also crosscut the Oligo-Miocene sedimentary beds locally (Jamali et al. 2010). Intermediate volcanic rocks are more abundant than acidic ones and pyroclastic deposits are lacking.

In the study area, several major NW–SE reverse faults displaced the flysch deposits (Mehrpartou 1997). The second set of N-S trending faults separate the intrusive body from adjacent units and the major deformation occurred along these faults, causing displacement and fracturing of the pluton (Mehrpartou 1997; Ferdowsi et al. 2015).

In general, post-Miocene volcanic rocks are concentrated in the southwestern part of the AAMZ but distribution of them in other parts of this zone is rare (Jamali et al. 2010). Andesite, trachyandesite, trachydacite, dacite, and rhyolite rocks are the
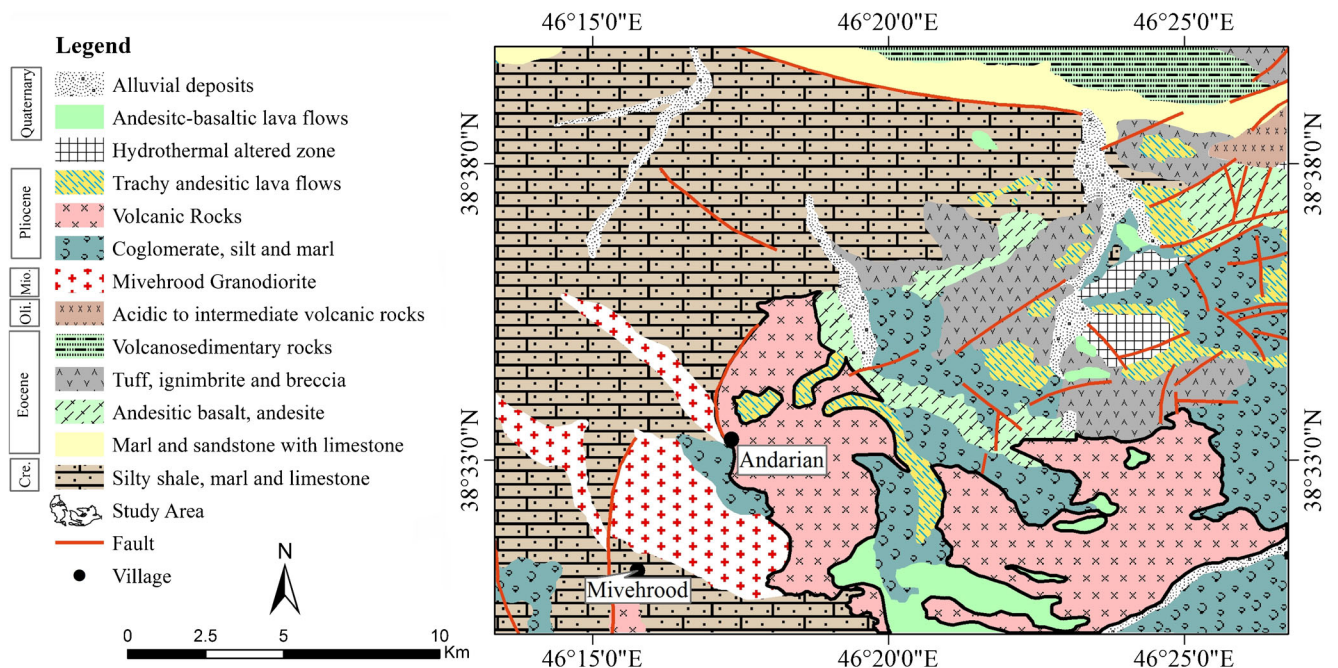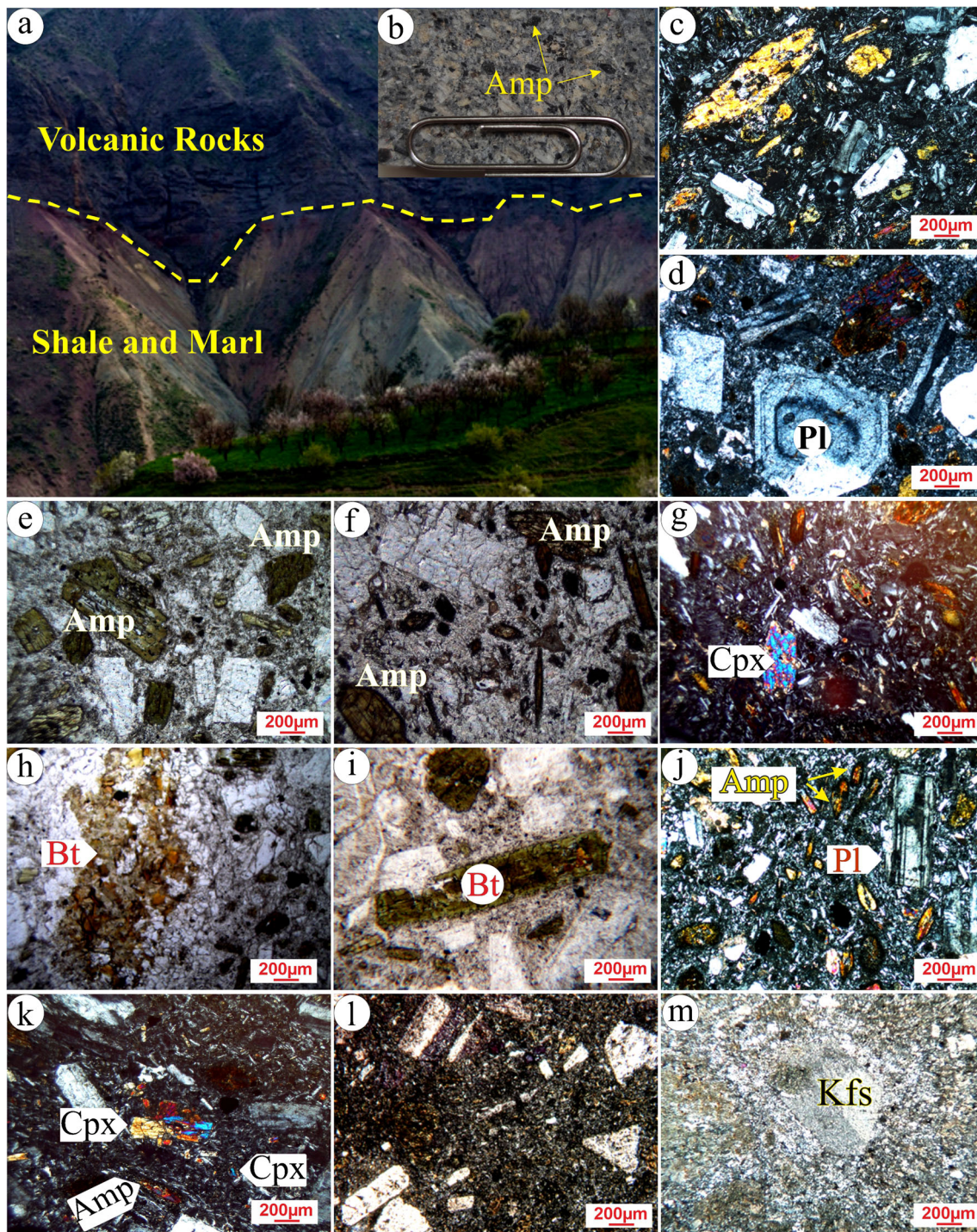

Fig. 2 Simplified geological map of the Andarian area after Mehrpartou (1997).

Fig. 3 a Stratigraphic contact of the Andarian volcanic rocks with the Oligo-Miocene sediments. **b** Handspecimen of hornblende andesite showing hornblende phenocrysts. **c** Microlitic porphyritic textures in hornblende andesite, crossed polarizers (XPL). **d** Zoned plagioclase phenocryst in hornblende andesite, XPL. **e** Semihedral green hornblende in hornblende andesite, parallel polarizers (PPL). **f** Brown hornblende in hornblende andesite, PPL. **g** Clinopyroxene phenocryst in the Andarian hornblende andesite, XPL. **h** Secondary biotite in hornblende andesite, PPL. **i** Amphibole is replaced by biotite in hornblende andesite, PPL. **j** Porphyritic texture in basaltic andesite, XPL. **k** Clinopyroxene crystals in two forms of phenocryst and matrix component in basaltic andesite, XPL. **l** Porphyritic to semi-trachytic texture in andesite, XPL. **m** Porphyric texture in rhyodacite, XPL. Mineral abbreviations are from Whitney and Evans (2010)

main constituent of post-Miocene volcanic rocks. Jamali et al. (2010) concluded that there are no clear genetic relationships between the post-Miocene volcanic rocks and the mineralization occurrences in the AAMZ. Based on extensive field observations, no mineralization associated with Neogene Andarian volcanic rocks has yet been reported.

Analytical method

The minerals were analyzed by using a fully automated JEOL JXA-8600 electron probe micro-analyzer at the Department of Earth and Environmental Sciences, Yamagata University, Japan. Selected points were analyzed using a 15-kV accelerating voltage and 20-nA beam current. The beam diameter was set to 5 μm and detection limits of 0.05 wt% with a maximum 40-s counting interval. Normalization for biotite, amphibole, plagioclase, and pyroxene was calculated on the basis of 24, 23, 8, and 6 oxygens per formula unit, respectively.

The volcanic rocks (8 samples) were powdered by agate mill for quantitative analysis of major and trace elements as well as rare earth elements. Major elements in samples were measured using an X-ray fluorescence spectrometer (XRF) using standard glass beads (these glass beads were prepared from whole rock powders) at SNU (Seoul National University). The glass beads that remain after measuring major element compositions using XRF were used to measure trace element compositions using laser ablation inductively coupled plasma mass spectrometry (LA-ICP-MS). Trace and rare earth elements content of the volcanic rocks were determined by LA-ICP-MS at KBSI (Korea Basic Science Institute). Helium gas, the laser ablation source gas, was applied at a typical flow rate of 0.701 L/min. The collected ICP-MS data were operated in time-resolved analysis for 100s and in the peak-hopping mode with a dwell time of 20 ms. The Nd:YAG laser was acquired at a 20-Hz repetition rate, 110-μm spot size, and 70% energy level (20 J/cm^2). More details of operating conditions of the laser source and ICP-MS were described in Kil and Jung (2015). Each bead was analyzed three times for monitoring the accuracy of data, and finally, the average was chosen as the analysis result. All data were normalized to calcium concentration, which was measured by the XRF as an internal standard.

Petrography of the volcanic rocks

The study area (Fig. 2) covered by the Pliocene volcanic rocks comprising basaltic andesite, andesite, hornblende andesite, and minor occurrences of dacite and rhyodacite.

Hornblende andesite

The hornblende andesite unit is one of the most widespread and dominant lithology in the Andarian area. The rocks show a porphyritic texture in hand specimens and contain visible phenocrysts of amphibole and plagioclase (Fig. 3b). Their color varies from greenish-gray to light gray. They are coarse- to medium-grained, with porphyritic and microlithic porphyritic textures (Fig. 3c). The hornblende andesites contain 27–53% (mean 33%) groundmass, 24–48% (mean 37%) plagioclase, 15–28% (mean 21%) amphibole, less than 10% clinopyroxene and biotite, and less than 4% magnetite and K-feldspar. Plagioclase (mainly 0.6–0.8 mm in size, maximum 2.4 mm long) and hornblende (mostly between 0.6 and 0.7 mm, maximum 1.6 mm) are the most abundant phenocrysts.

Plagioclase crystals are mostly subhedral and zoned (Fig. 3d), whereas hornblendes are often subhedral to euhedral in shape. Hornblende phenocrysts show both deep green and brown color (Fig. 3e, f). Clinopyroxene crystals are only observed in few thin sections as phenocrysts (Fig. 3g), occasionally showing replacement by amphibole (see also in mineral chemistry evidence). Clinopyroxenes together with plagioclase grains developed glomeroporphyritic texture. The groundmass is composed of microlites but in some thin sections glass is preserved. Primary biotite is rare but it can be found as secondary biotite, which often replaces amphibole (Fig. 3h, i).

Basaltic andesite

Basaltic andesite is another major lithotype in the area. Coarse-grained plagioclase (mean 30%) together with hornblende (mean 13%) and clinopyroxene (mean 8%) and minor amount of fine-grained pyroxene and microlite in matrix (45%) yield a porphyritic texture (Fig. 3j, k). The subhedral to anhedral pale-green clinopyroxenes, variable in size, lack zoning. The hornblendes (mostly >400 μm) form elongated rod-shaped crystals (Fig. 3j), subhedral columnar, and large idiomorphic grains lacking a clear zoning. Plagioclase grains (>200 μm) sometimes exhibit zoning and tapered twins (lamellar becomes gradually thinner and narrower; Fig. 3j). Biotite, the less abundant ferromagnesian mineral, with brown to dark brown color is present in some cases and titanite is also observed as an accessory mineral.

Andesite

The andesites display porphyritic to semi-trachytic textures (Fig. 3l). Plagioclase (mean 45%, mainly 0.4–0.6 mm) and hornblende phenocrysts show some orientation probably related to the lava flow. Andesites are slightly altered as most of the plagioclases show weak sericitic-kaolinitic alteration. Hornblende crystals are partially altered to chlorite and aggregate clusters of secondary biotite. K-feldspar crystals are only observed in few thin sections.

Dacite and rhyodacite

The dacite and rhyodacite hand specimens are milky to cream in color. Because of the apparent similarity of the two rock

types, dacites and rhyodacites are difficult to discriminate in hand specimen. The rhyodacite shows a porphyritic texture and mainly consists of quartz, alkali feldspar, biotite, and minor amounts of zircon, Fe–Ti oxides, and secondary biotite (Fig. 3m). Some samples display signs of chloritization and sericitization. The dacites contain amphibole and plagioclase phenocrysts in a groundmass of quartz and feldspar. Completely unaltered samples of dacite and rhyodacite were not observed, most of them partially altered.

Result

Mineral composition

In this section, we present mineral composition of feldspar, amphibole, clinopyroxene, and biotite that were analyzed in representative samples of hornblende andesite and basaltic andesite rocks.

Feldspar

Representative feldspar analyses and their normalized values of two types of rock samples are presented in Tables 1 and 2. Plagioclases in the hornblende andesites show a compositional range from albite to andesine ($An_{5.1-33.8}$; majority recognized as oligoclase). This range overlaps with that of basaltic andesite plagioclases ($An_{11.9-37.0}$; Fig. 4a). The point analyses of K-feldspar crystals suggest sanidine and anorthoclase variants (Fig. 4a).

As mentioned in the petrographic section, zoning in plagioclase crystals is common. All the zoning in the studied phenocrysts shows some coarse oscillations (>10 μm) with moderate anorthite variation (~4 mol%; Fig. 4b; Table 2).

Amphibole

The chemical composition, normalized to 23 oxygens, of the analyzed amphiboles from the hornblende andesites and basaltic andesites is listed in Table 3. Based on BSE images, amphiboles are often found as unaltered phenocrysts and microcrysts and there is no clear zoning in them. Almost all of the amphiboles are primary and have high TiO_2 content (1.01–3.77 wt% in the hornblende andesite and 1.12–3.70 wt% in the basaltic andesite). Based on the Leake et al. (2004) classification, all amphiboles of the volcanic rocks have Ca + Na > 1.00 implying that they are calcic amphiboles. Regarding calcic amphibole classification (Leake et al. 2004; Hawthorne et al. 2012), most of the amphiboles are edenite and pargasite/hastingsite. Few samples also show magnesio-hornblende and tschermakite by plotting their composition (Fig. 5).

Pyroxene

The result of point analysis of the hornblende andesite and basaltic andesite samples is reported in Table 4. The clinopyroxene compositions are plotted in the quad field (Morimoto 1988; Fig. 6a). Figure 6 b presents the Wo–En–Fs diagram suggesting diopside and augite species for clinopyroxenes (Morimoto 1988).

Mica

As mentioned earlier, the amount of mica crystals in the studied volcanic rocks is insignificant. The result of the point analyses of mica is reported in Table 5. Al_2O_3 and TiO_2 contents of mica vary between 12.97 to 17.90 wt% and 0.49 to 4.87 wt% respectively (Table 5). Based on Al versus Fe#= Fe/(Fe + Mg) diagram (Foster 1960), all biotites from the hornblende andesite and basaltic andesite are plotted in the phlogopite field (Fig. 7a). Furthermore, using ternary classification diagram of biotite (Foster 1960), all analyses are plotted either in or at the border of the phlogopite field (Fig. 7b).

Thermobarometry

Experimental investigation demonstrates that amphibole and clinopyroxene composition can be used to estimate the P-T condition of the volcanic rock crystallization (Johnson and Rutherford 1989; Putirka 2008; Ridolfi et al. 2010; Neave and Putirka 2017).

The thermobarometry equations (Ridolfi et al. 2010; Ridolfi and Renzulli 2012) which were developed for calcic amphiboles of volcanic calc-alkaline rocks are used in this paper. In the equations, the amphiboles with less than 10% CaO are assumed as low calcic amphiboles that are not able to measure the temperature and pressure. According to these thermobarometric equations (Ridolfi et al. 2010), the amphibole composition of the hornblende andesite suggests an estimated range of temperatures of 809–1013°C (mean = 914 ± 47°C) and pressures of 0.77–3.81 kbar (mean = 2.04 ± 0.22 kbar; Fig. 8a, Table 3). The P–T diagram of Ridolfi et al. (2010) has been divided into four domains (Fig. 8a): (1) (Mg-Hbl + Pl ± Opx ± Mgn ± Ilm ± Bt), (2) (Tsc-Prg + Pl ± Cpx ± Opx ± Mgn ± Ilm), (3) (Tsc-Prg ± Pl ± Ol ± Cpx ± Opx ± Mgn ± Ilm), and (4) (Cpx ± Mgn ± Ol ± Pl). The samples plot within domains 1 to 3, so that all of the minerals with the exception of orthopyroxene, olivine, and ilmenite are also observed in petrographic studies. The equation of Ridolfi et al. (2010) yields estimated temperatures of 853–1014°C (mean = 946 ± 46 °C) and pressures of 0.89 to 3.87 kbar (mean = 2.41 ± 0.26 kbar) for the basaltic andesite samples (Fig. 8a).

Moreover, amphibole-plagioclase geothermometry (Holland and Blundy 1994) and Al-in-hornblende

Table 1 Representative chemical compositions and calculated mineral formulae of the feldspars from the Andarian volcanic rocks. Oxides are in wt% and elements are in a.p.f.u., *bdl* below detection limit

Sample number	AN-40-19-4	AN-41-19	AN-72-31	AN-41-4	AN-44-21-3	AN-48-12-4	AN-40-12	AN-40-13	AN-40-13-3	AN-40-14	AN-40-14-3	AN-43-4	AN-40-5	AN-5-2	AN-40-6-2	AN-40-12	AN-40-12-2	AN-40-14	AN-40-14-3	AN-40-18
SiO_2	62.99	62.25	67.21	57.27	63.24	55.68	60.18	62.10	63.44	60.35	62.04	61.44	59.21	62.19	58.75	60.18	62.79	60.35	62.04	61.06
TiO_2	0.08	0.07	bdl	0.05	0.05	bdl	bdl	bdl	0.07	bdl	0.06	bdl	bdl	0.06	bdl	bdl	bdl	bdl	0.06	0.06
Al_2O_3	19.38	22.55	20.45	26.29	21.30	26.43	24.13	22.51	22.36	24.51	23.52	21.80	24.88	22.33	25.08	24.13	22.72	24.51	23.52	22.82
FeO^*	0.60	0.30	0.12	0.35	0.46	0.55	0.20	0.26	0.21	0.22	0.35	0.30	0.39	0.37	0.42	0.20	0.28	0.22	0.35	0.24
MnO	bdl	bdl	bdl	bdl	bdl	0.23	bdl	bdl	bdl	bdl	bdl	bdl	bdl	bdl	bdl	bdl	bdl	bdl	bdl	bdl
MgO	bdl	bdl	bdl	bdl	bdl	bdl	bdl	bdl	bdl	bdl	bdl	bdl	bdl	bdl	bdl	bdl	bdl	bdl	bdl	bdl
CaO	1.05	3.33	1.05	7.95	2.52	8.87	5.62	4.30	3.43	5.93	4.52	4.07	6.97	4.06	6.54	5.62	4.46	5.93	4.52	4.34
Na_2O	5.88	10.48	12.78	7.16	10.25	7.53	8.10	8.68	7.54	8.73	8.41	8.73	7.80	8.05	7.96	8.10	8.09	8.73	8.41	9.71
K_2O	10.75	1.41	0.23	0.61	0.05	0.04	0.93	1.34	1.82	0.84	1.44	1.86	0.66	1.32	0.98	0.93	1.72	0.84	1.44	1.04
Total	100.74	100.39	101.83	99.68	97.88	99.32	99.15	99.20	98.87	100.57	100.33	98.19	99.90	98.39	99.73	99.15	100.05	100.57	100.33	99.27
Normalization based on 8 O																				
Si	2.501	2.480	2.600	2.297	2.610	2.241	2.427	2.504	2.567	2.400	2.473	2.502	2.370	2.528	2.355	2.427	2.509	2.400	2.473	2.460
Ti	0.003	0.003	0.000	0.002	0.002	bdl	bdl	bdl	0.003	bdl	0.002	bdl	bdl	0.002	0.002	bdl	bdl	bdl	0.002	0.002
Al	1.026	1.198	1.055	1.406	1.172	1.418	1.298	1.210	1.206	1.299	1.250	1.184	1.328	1.210	1.341	1.298	1.211	1.299	1.250	1.226
Fe_{total}	0.047	0.024	0.009	0.028	0.038	0.044	0.016	0.021	0.017	0.017	0.028	0.024	0.031	0.030	0.033	0.016	0.023	0.017	0.028	0.019
Mn	bdl	bdl	bdl	bdl	bdl	0.018	bdl	bdl	bdl	bdl	bdl	bdl	bdl	bdl	bdl	bdl	bdl	bdl	bdl	bdl
Ca	0.083	0.265	0.117	0.638	0.208	0.714	0.453	0.347	0.278	0.472	0.360	0.331	0.558	0.330	0.525	0.453	0.356	0.472	0.360	0.350
Na	0.934	1.670	2.148	1.149	1.528	1.212	1.306	1.400	1.220	1.388	1.341	1.422	1.249	1.309	1.277	1.306	1.293	1.388	1.341	1.565
K	1.707	0.225	0.035	0.098	0.009	0.006	0.150	0.216	0.295	0.133	0.229	0.303	0.105	0.215	0.157	0.150	0.275	0.133	0.229	0.167
Or	62.66	10.43	1.51	5.19	0.50	0.29	7.86	11.00	16.46	6.68	11.87	14.73	5.50	11.59	7.99	7.86	14.30	6.68	11.87	8.03
Ab	34.28	77.29	93.41	60.97	87.57	62.75	68.42	71.32	68.05	69.65	69.46	69.16	65.32	70.59	65.21	68.42	67.19	69.65	69.46	75.15
An	3.06	12.28	5.07	33.84	11.93	36.96	23.73	17.68	15.48	23.67	18.67	16.11	29.18	17.82	26.80	23.73	18.51	23.67	18.67	16.81
Location	rim	core	rim	core			core	core	rim	core	rim	core	core	core	core	core	core	core	rim	rim

Table 2 Chemical compositions and calculated mineral formulae of the feldspars from the Andarian volcanic rocks. Bold values are representative points of plagioclase zoning

Sample number	AN-46-7-3	AN-46-9-3	AN-46-23	AN-46-24-2	AN-48-12-2	AN-48-13-2	AN-48-24-6-1	AN-48-24-6-2	AN-48-24-6-3	AN-48-24-6-4	AN-48-24-6-5	AN-48-32-3	AN-49-4	AN-49-4-2	AN-49-4-3	AN-49-13-2	AN-49-20-3	AN-49-9-9	AN-49-9-4
SiO_2	60.41	63.19	58.04	63.22	60.78	58.85	**59.60**	**59.75**	**57.72**	**60.93**	**59.97**	62.22	57.69	56.94	58.63	60.21	60.19	59.02	60.86
TiO_2	bdl	bdl	bdl	0.10	bdl	bdl	**bdl**	**bdl**	**bdl**	**bdl**	**bdl**	bdl	bdl	bdl	bdl	0.06	bdl	bdl	bdl
Al_2O_3	24.23	22.05	28.54	22.29	23.79	25.21	**24.47**	**24.16**	**25.94**	**22.79**	**23.71**	22.44	24.67	25.29	23.92	24.92	23.01	23.52	23.09
FeO*	0.24	0.30	0.25	0.70	0.21	0.16	**0.20**	**0.20**	**0.23**	**0.23**	**0.25**	0.25	0.24	0.34	0.23	0.28	0.24	0.33	0.41
MnO	bdl	bdl	bdl	bdl	bdl	bdl	**bdl**	**bdl**	**bdl**	**0.15**	**bdl**	0.12	bdl	0.08	bdl	0.08	0.08	bdl	bdl
MgO	bdl	bdl	bdl	0.90	bdl	bdl	**bdl**	**bdl**	**bdl**	**bdl**	**bdl**	bdl	bdl	bdl	bdl	0.05	bdl	bdl	bdl
CaO	4.63	2.71	7.51	3.56	5.36	7.01	**6.16**	**5.67**	**7.72**	**4.77**	**5.15**	3.89	6.43	7.52	6.35	6.16	4.69	5.81	4.97
Na_2O	10.33	10.92	7.99	6.12	9.86	9.11	**9.60**	**8.97**	**8.77**	**8.72**	**9.43**	10.57	9.30	8.53	9.41	8.92	9.45	9.34	9.81
K_2O	0.85	1.56	0.38	4.45	bdl	bdl	**bdl**	**0.06**	**0.09**	**bdl**	**bdl**	bdl	bdl	bdl	bdl	bdl	bdl	bdl	bdl
Total	100.69	100.72	102.71	101.34	100.00	100.34	**100.03**	**98.81**	**100.47**	**97.59**	**98.50**	99.49	98.34	98.70	98.54	100.67	97.67	98.01	99.14
Normalization based on 8 O																			
Si	2.399	2.509	2.259	2.495	2.431	2.346	**2.383**	**2.417**	**2.296**	**2.497**	**2.435**	2.501	2.345	2.306	2.379	2.392	2.465	2.408	2.454
Ti	bdl	bdl	bdl	0.004	bdl	bdl	**bdl**	**bdl**	**bdl**	**bdl**	**bdl**	bdl	bdl	bdl	bdl	0.002	bdl	bdl	bdl
Al	1.283	1.167	1.481	1.173	1.269	1.340	**1.305**	**1.303**	**1.375**	**1.245**	**1.283**	1.203	1.337	1.366	1.294	1.320	1.256	1.279	1.241
Fe_{total}	0.019	0.024	0.019	0.055	0.017	0.013	**0.016**	**0.016**	**0.018**	**0.018**	**0.020**	0.020	0.020	0.028	0.018	0.022	0.020	0.027	0.033
Mn	bdl	bdl	bdl	bdl	bdl	bdl	**bdl**	**bdl**	**bdl**	**0.012**	**0.000**	0.010	bdl	0.007	bdl	0.006	0.006	bdl	bdl
Mg	bdl	bdl	bdl	0.071	bdl	bdl	**bdl**	**bdl**	**bdl**	**bdl**	**bdl**	bdl	bdl	bdl	bdl	0.003	bdl	bdl	bdl
Ca	0.368	0.215	0.584	0.281	0.429	0.559	**0.492**	**0.459**	**0.614**	**0.391**	**0.418**	0.313	0.523	0.609	0.515	0.489	0.384	0.474	0.401
Na	1.640	1.734	1.244	0.966	1.576	1.453	**1.535**	**1.452**	**1.395**	**1.430**	**1.531**	1.700	1.512	1.382	1.527	1.418	1.548	1.524	1.582
K	0.135	0.248	0.060	0.702	bdl	bdl	**0.000**	**0.009**	**0.014**	**bdl**	**bdl**	bdl	bdl	bdl	bdl	bdl	bdl	bdl	bdl
Or	6.28	11.27	3.16	36.03	0.06	0.00	**0.00**	**0.48**	**0.69**	**0.11**	**0.00**	0.01	0.12	0.21	0.10	0.46	0.00	0.02	0.21
Ab	76.55	78.94	65.89	49.56	78.56	72.22	**75.71**	**75.62**	**68.94**	**78.44**	**78.55**	84.46	74.21	69.27	74.71	74.01	80.12	76.26	79.61
An	17.17	9.79	30.95	14.42	21.37	27.78	**24.29**	**23.90**	**30.36**	**21.45**	**21.46**	15.53	25.67	30.52	25.19	25.53	19.88	23.72	20.18
Location	rim	rim	core		core	core	**core**	**core**	**core**	**rim**	**rim**	core	core	core	rim	core	rim	core	rim

Fig. 4 a Composition of feldspars of the Andarian volcanic rocks in the Ab-Or-An diagram (Deer et al. 1992). **b** Representative core to rim profiles of An (mol%) for the plagioclase phenocrysts with the photomicrograph and BSE image
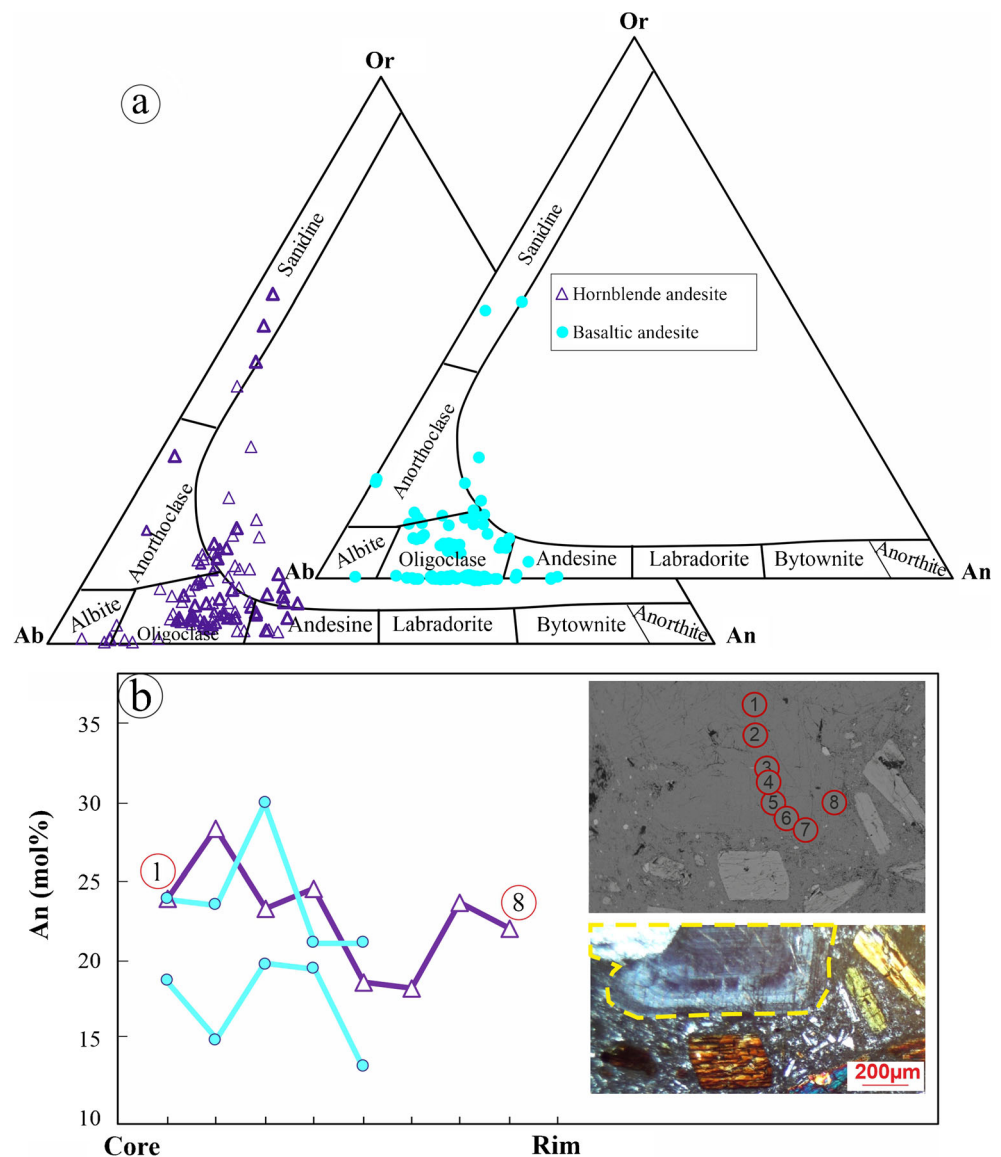
geobarometry (Anderson and Smith 1995) give temperatures from 710 to 892°C (mean = 816 °C) and pressures of 0.8–2.9 kbar (mean = 1.7 kbar) for the hornblende andesites. These equations yield temperatures of 707–899°C (mean = 826 °C) and pressures of 0.5 to 2.8 kbar (mean = 1.6 kbar) for the basaltic andesite samples (Table 6). We also applied classic thermobarometry (e.g., Saki et al. 2021) using the Ti-in-hornblende thermometric (Otten 1984) and the Al [VI]-in-hornblende (Larocque and Canil 2010) barometric equations. Pressures calculated with the calibration of Larocque and Canil (2010) are from 0.5 to 3.4 kbar (mean = 1.5 kbar) and 0.4–3.5 kbar (mean = 1.7 kbar) for the hornblende andesites and basaltic andesites, respectively. The obtained temperatures range from 762 to 957 °C (mean = 879 °C) and 774–959 °C (mean = 872 °C) using calculation of Otten (1984) for

the hornblende andesites and basaltic andesites, respectively (Table 6).

A qualitative estimate of clinopyroxene crystallization pressure can be obtained using the Al^{IV} vs. Al^{VI} diagram (Aoki and Shiba 1973). All the samples are clustered in the low- to medium-pressure field (Fig. 8b). The XPT vs. YPT diagram of Soesoo (1997) suggests quantitative temperature of 1175–1250°C for clinopyroxene (Fig. 8c).

The occurrence of remarkably high amounts of amphibole in the studied andesites indicates that the Andarian volcanic rocks crystallized from a relatively water-rich magma. Ridolfi et al. (2010) provide a method for estimating the water contents on the basis of the amphibole composition. These estimates indicate water contents of magma up to 4.89 wt% for the hornblende andesite and up to 3.61 wt% for the basaltic

Table 3 Representative chemical compositions and calculated mineral formulae of the amphiboles from the Andarian volcanic rocks

Sample number	AN-41-7-4	AN-72-3	AN-72-3-4	AN-72-3-2	AN-41-1-3	AN-50-14-2	AN-50-14	AN-43-16	AN-43-10-1	AN-41-10	AN-41-9	AN-50-24-2	AN-50-23	AN-40-10-3	An-40-10-2	AN-43-11-1	AN-72-16	AN-72-16	AN-50-11
SiO_2	41.94	47.84	47.56	46.97	43.18	43.20	41.12	40.48	41.24	44.09	40.90	47.87	48.88	42.16	42.40	41.37	48.94	47.74	41.81
TiO_2	2.95	1.62	1.31	1.34	2.17	3.14	3.33	3.63	2.91	2.33	3.13	1.51	1.27	2.91	2.83	3.03	1.11	1.40	3.77
Al_2O_3	12.16	6.99	7.29	7.64	11.10	10.24	11.56	11.38	11.87	9.16	11.61	6.75	5.65	11.47	11.73	11.79	6.35	7.69	12.18
Cr_2O_3	bdl	bdl	bdl	bdl	0.07	bdl	bdl	bdl	bdl	bdl	bdl	bdl	0.07	bdl	0.07	bdl	bdl	0.05	bdl
FeO*	11.99	9.47	11.95	12.05	10.84	10.99	12.36	10.23	9.06	13.35	10.49	11.15	10.66	10.30	7.50	8.41	11.60	12.24	11.60
MnO	0.19	0.26	0.23	0.29	0.11	0.15	0.18	0.05	0.11	0.20	0.13	0.39	0.34	0.11	0.18	0.10	0.24	0.31	0.17
MgO	14.86	15.68	15.36	15.56	15.20	14.81	13.22	14.80	15.73	14.18	15.14	16.00	16.26	15.60	16.64	16.32	16.18	14.53	13.08
CaO	11.68	12.55	11.63	11.70	11.84	12.32	12.73	11.63	11.80	11.50	11.64	11.77	12.01	11.83	11.55	11.85	11.73	11.69	11.07
Na_2O	3.68	2.54	2.41	2.67	3.25	3.68	4.09	3.54	3.17	3.09	3.52	2.84	2.51	3.64	3.34	3.20	2.53	2.77	4.30
K_2O	0.95	0.47	0.49	0.59	0.78	0.64	0.83	0.82	1.35	0.75	0.82	0.54	0.43	0.93	1.24	1.57	0.45	0.47	0.65
F	bdl	0.38	0.11	bdl	0.26	0.18	0.32	0.97	0.13	0.37	0.31	0.76	0.31	0.68	0.45	0.38	0.49	0.49	0.54
Cl	bdl	bdl	bdl	bdl	bdl	bdl	bdl	bdl	bdl	bdl	bdl	bdl	bdl	bdl	bdl	bdl	bdl	bdl	bdl
Total	100.40	97.81	98.35	98.81	98.80	99.34	99.73	97.51	97.36	99.02	97.70	99.59	98.40	99.63	97.90	98.03	99.63	99.39	99.17
Normalization based on 23 O																			
Si	6.000	6.953	6.851	6.747	6.252	6.297	6.062	6.029	6.054	6.432	6.014	6.877	7.061	6.101	6.150	6.044	6.968	6.779	6.045
Ti	0.318	0.178	0.142	0.144	0.237	0.344	0.369	0.406	0.321	0.255	0.347	0.163	0.138	0.317	0.309	0.333	0.119	0.150	0.410
Al_{IV}	2.000	1.047	1.149	1.253	1.748	1.703	1.938	1.971	1.946	1.568	1.986	1.123	0.939	1.899	1.850	1.956	1.032	1.221	1.955
Al_{VI}	0.051	0.151	0.088	0.040	0.147	0.056	0.071	0.026	0.108	0.006	0.025	0.020	0.023	0.057	0.154	0.073	0.033	0.065	0.120
Cr	bdl	bdl	bdl	bdl	0.008	bdl	bdl	bdl	bdl	bdl	bdl	bdl	0.008	bdl	0.008	bdl	bdl	0.006	bdl
Fe^{3+}	0.533	0.000	0.421	0.470	0.390	0.000	0.000	0.242	0.327	0.441	0.439	0.261	0.131	0.344	0.314	0.307	0.397	0.443	0.000
Fe^{2+}	0.901	1.151	1.019	0.977	0.923	1.340	1.524	1.032	0.785	1.188	0.850	1.079	1.156	0.902	0.596	0.720	0.984	1.011	1.406
Mn	0.022	0.032	0.028	0.036	0.014	0.018	0.023	0.006	0.014	0.024	0.016	0.047	0.041	0.014	0.022	0.012	0.029	0.037	0.021
Mg	3.170	3.398	3.299	3.331	3.282	3.218	2.905	3.286	3.443	3.084	3.319	3.427	3.502	3.365	3.598	3.554	3.435	3.288	3.034
Ca	1.790	1.955	1.795	1.801	1.836	1.924	2.011	1.856	1.856	1.797	1.834	1.811	1.859	1.835	1.795	1.855	1.790	1.779	1.838
Na	1.022	0.716	0.673	0.743	0.914	1.040	1.169	1.021	0.903	0.873	1.004	0.791	0.704	1.021	0.938	0.907	0.699	0.763	1.228
K	0.173	0.087	0.090	0.108	0.143	0.118	0.156	0.157	0.252	0.140	0.153	0.100	0.080	0.172	0.229	0.293	0.082	0.086	0.120
F	bdl	0.176	0.050	bdl	0.120	0.083	0.151	0.455	0.059	0.172	0.145	0.345	0.140	0.312	0.205	0.176	0.222	0.218	0.245
Mg/(Mg+Fe)	0.779	0.747	0.764	0.773	0.781	0.706	0.656	0.761	0.814	0.722	0.796	0.761	0.752	0.789	0.858	0.831	0.777	0.765	0.683
T (°C)	1002	857	834	854	877	952	979	1008	1012	909	1008	839	809	991	1001	1013	814	838	995
P (MPa)	367	109	114	123	100	242	354	339	368	185	346	99	77	320	343	356	89	126	381
$\log fO_2$	−9.54	−11.44	−11.65	−11.26	−10.49	−10.38	−10.43	−9.56	−9.06	−10.93	−9.35	−11.55	−11.98	−9.47	−9.00	−8.88	−11.83	−12.01	−10.13
H_2O melt (wt.%)	3.05	3.88	3.59	3.05	2.65	2.95	3.22	2.74	2.19	2.88	2.94	2.42	2.48	4.89	2.27	1.29	2.85	4.05	3.42
Location	rim	rim	rim	core	core	rim	core	core	core	core	core	rim	core	rim	core	core	rim	core	rim

Fig. 5 Amphibole classification diagram (Hawthorne et al. 2012) of the Andarian volcanic rocks. Symbols as in Fig. 4
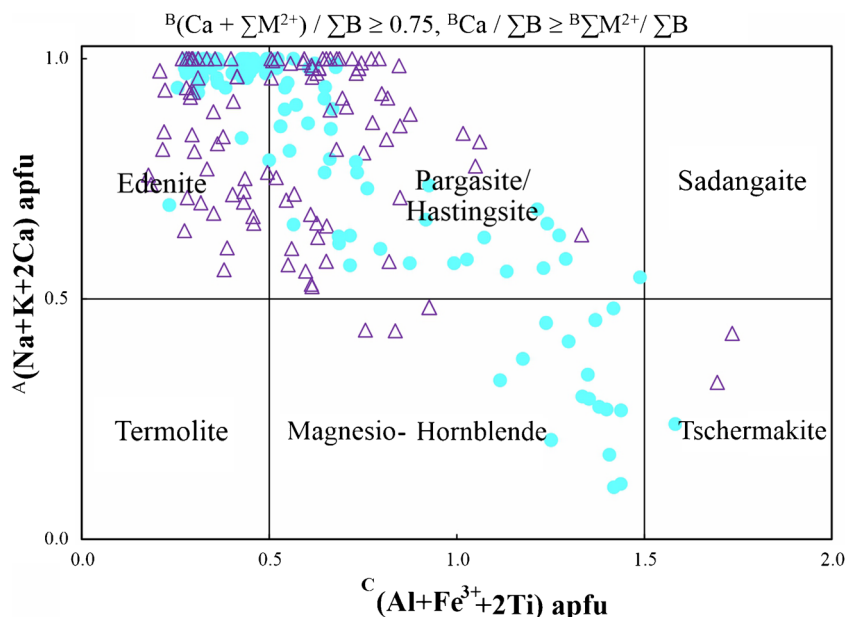
andesite. These findings appear to support the hypothesis that primary melt was water-rich.

Oxygen fugacity and magma source

The amphibole composition can reflect the physico-chemical conditions of the magma (Ridolfi et al. 2010). Anderson and Smith (1995) proposed that the Fe# (Fe/Fe + Mg) of amphibole reflect the oxygen fugacity of the melt. Since Fe/Fe + Mg ratios of the Andarian amphibole are less than 0.6, it is inferred that amphiboles crystallized at highly oxidizing conditions (Fig. 9a). Quantitative calculation of oxygen fugacity from the amphiboles was conducted using Ridolfi et al.'s (2010) equation. Log fO_2 values for the hornblende andesite and basaltic andesite range from −8.8 to −12 and −8.7 to −11.1 bars, respectively. The distribution of these samples in temperature vs. log fO_2 diagram indicates that all samples plot between NNO and NNO+2 buffers and follow their trend (Fig. 9b).

The clinopyroxene data of the Andarian volcanics are placed above the line of $Fe^{3+} = 0$ on the $Al^{VI}+2Ti+Cr$ vs. $Na + Al^{IV}$ diagram of Schweitzer et al. (1979), meaning that the pyroxenes have been formed at high oxygen fugacity (Fig. 9c). This result is also confirmed by the oxygen fugacity estimation using amphibole chemistry.

The plot of the amphibole data on the Al_2O_3 vs. TiO_2 magma source discriminator diagram (Changyi and Sanyuan 1984) suggests a mantle and crust-mantle as the likely source for the Andarian volcanic rocks (Fig. 10a). In addition, MgO vs. $FeO^*/(FeO^* + MgO)$ diagram for biotite (Zhou 1986) shows the mantle source for these samples (Fig. 10b).

Whole rock geochemistry

Table 7 illustrates the whole rock analysis data for major and trace elements of 8 volcanic rocks from the Andarian region. Although in the major element analyses of volcanic rocks the total volatile content has been reported as loss on ignition (LOI), the elimination of volatile content in order to monitor alteration effect is normal (Gill 2010). All data have been recalculated into the volatile free form before plotting on the related diagrams.

Based on petrographic studies and LOI content, the samples are classified to fresh (LOI<1%), relatively fresh (LOI<2%), or slightly altered (2<LOI<5%). Analyzed samples are characterized by relatively moderate amounts of SiO_2 (60.88–70.75 wt%), limited range of Al_2O_3 (15.12–16.58 wt%), low TiO_2 (0.43–0.84 wt%), high Na_2O (4.50–5.20 wt%), and variable contents of Fe_2O_3 and MgO (2.13–5.06 wt% and 1.56–3.86 wt% respectively). The relatively low LOI content (mean~2.4) reflects a relatively low effect of alteration in these samples.

In the Zr/TiO_2 vs. SiO_2 diagram (Winchester and Floyd 1977), the Andarian volcanic rocks plot in the fields of andesite and rhyodacite-dacite, whereas in Ti vs. Zr plot (Hallberg 1984) all samples fall into the andesite field (Fig. 11a, b). The geochemical classification diagrams mostly match classifications obtained by using petrographic nomenclature, except for rhyodacite samples which classify as andesite in the Ti vs. Zr graph (Hallberg 1984).

As mentioned in the petrographic section, the rhyodacitic samples are more or less affected by hydrothermal alteration. Since REEs are not completely immobile (e.g., Zhiwei and Zhenhua 2003; Dongen et al. 2010; Hikov 2011), they may

Table 4 Representative chemical compositions and calculated mineral formulae of the clinopyroxenes from the Andarian volcanic rocks

Sample number	AN-42-5	AN-42-11	AN-42-12	AN-42-12-2	AN-42-12-3	AN-42-17-3	AN-44-2-2	AN-44-9-2	AN-44-14	AN-44-24	AN-44-26	AN-44-27	AN-48-20	AN-48-21-2	AN-48-22	An-46-10	An-46-18-2	An-46-19	An-46-19-3	An-46-21-3
SiO$_2$	50.82	50.01	51.62	51.21	51.51	51.49	51.16	52.01	49.32	50.88	49.31	51.72	50.14	49.68	50.83	54.14	53.90	54.45	53.03	52.93
TiO$_2$	0.85	1.12	0.29	0.19	0.54	0.37	0.61	0.41	1.11	0.27	0.83	0.52	0.64	0.81	0.58	0.61	0.58	0.24	0.54	0.69
Al$_2$O$_3$	2.30	3.44	1.15	1.06	1.93	1.61	1.87	2.12	4.23	1.01	3.94	1.88	2.88	3.51	2.31	2.35	3.48	2.91	3.78	3.81
Cr$_2$O$_3$	bdl	bdl	bdl	bdl	bdl	bdl	bdl	0.59	0.07	bdl	0.83	0.40	0.40	0.41	0.10	bdl	0.05	0.39	0.19	bdl
FeO*	6.81	6.13	9.28	8.84	5.54	8.35	5.95	4.46	6.20	8.35	4.56	5.17	4.94	5.58	6.48	6.07	5.38	4.00	5.88	6.06
MnO	0.16	0.07	0.22	0.32	0.11	0.19	0.08	bdl	bdl	0.08	bdl	bdl	bdl	bdl	bdl	0.41	0.15	bdl	0.09	bdl
MgO	16.15	15.25	14.80	14.25	17.09	15.81	16.99	17.63	15.24	14.78	15.85	17.77	15.86	16.06	17.19	16.02	16.43	17.16	15.00	15.54
CaO	22.48	23.49	21.91	22.09	22.20	21.96	22.63	22.26	23.23	21.76	23.14	22.03	23.30	22.65	21.37	17.87	18.20	17.21	18.72	17.72
Na$_2$O	0.57	0.78	0.92	1.08	0.48	0.69	0.43	0.70	0.52	1.02	0.68	0.43	0.66	0.66	0.52	0.76	0.69	1.09	0.82	0.78
K$_2$O	bdl	0.07	bdl	bdl	bdl	bdl	0.61	0.41	1.11	0.27	0.83	0.52	0.64	0.81	0.58	bdl	bdl	bdl	bdl	bdl
Total	100.14	100.36	100.19	99.04	99.40	100.47	100.33	100.59	101.03	98.42	99.97	100.44	99.46	100.17	99.96	98.23	98.86	97.45	98.05	97.53
Normalization based on 6 O																				
Si	1.861	1.825	1.905	1.911	1.889	1.887	1.859	1.873	1.787	1.904	1.795	1.871	1.837	1.808	1.872	2.020	1.990	2.020	1.982	1.981
Ti	0.023	0.031	0.008	0.005	0.015	0.010	0.017	0.011	0.030	0.008	0.023	0.014	0.020	0.022	0.016	0.024	0.021	0.010	0.011	0.023
Al$_{IV}$	0.141	0.142	0.100	0.090	0.110	0.120	0.141	0.139	0.212	0.100	0.193	0.126	0.160	0.187	0.130	0.098	0.031	0.000	0.036	0.042
Al$_{VI}$	0.004	0.006	0.050	0.040	0.030	0.050	0.062	0.061	0.030	0.051	0.040	0.053	0.151	0.040	0.040	0.002	0.119	0.127	0.129	0.126
Cr	bdl	bdl	bdl	bdl	bdl	bdl	bdl	0.017	0.002	bdl	0.024	0.011	0.008	0.012	0.010	bdl	0.001	0.001	0.011	bdl
Fe total	0.208	0.187	0.286	0.276	0.170	0.256	0.181	0.134	0.188	0.261	0.139	0.156	0.165	0.170	0.161	0.190	0.171	0.123	0.184	0.190
Mn	0.005	0.002	0.007	0.010	0.004	0.006	0.002	bdl	bdl	0.003	bdl	bdl	bdl	bdl	bdl	0.010	0.005	0.003	0.001	bdl
Mg	0.881	0.830	0.814	0.793	0.934	0.863	0.921	0.947	0.823	0.824	0.860	0.959	0.848	0.870	0.951	0.890	0.922	0.950	0.841	0.873
Ca	0.882	0.918	0.866	0.883	0.872	0.862	0.881	0.859	0.902	0.873	0.903	0.854	0.876	0.883	0.834	0.710	0.719	0.682	0.750	0.710
Na	0.041	0.055	0.066	0.078	0.034	0.049	0.030	0.049	0.036	0.074	0.048	0.030	0.049	0.047	0.036	0.048	0.053	0.081	0.062	0.060
K	bdl	0.003	bdl	bdl	bdl	bdl	0.028	0.019	0.051	0.013	0.039	0.024	0.035	0.038	0.027	bdl	0.001	0.001	0.011	bdl
Wo	49.11	52.53	48.90	50.53	47.66	48.15	48.90	47.58	52.28	50.30	51.20	47.11	51.37	50.35	47.25	39.80	40.22	38.93	42.37	40.20
En	49.08	47.47	45.97	45.37	51.04	48.22	51.10	52.42	47.72	47.52	48.80	52.89	48.63	49.65	52.75	49.64	50.51	54.01	47.24	49.07
Fs	1.81	0.00	5.13	4.10	1.30	3.63	0.00	0.00	0.00	2.18	0.00	0.00	0.00	0.00	0.00	10.56	9.28	7.06	10.38	10.73
Location	core	core	core	core	rim	rim	core	core	core	core	core	core	core	rim	core	core	core	core	rim	rim
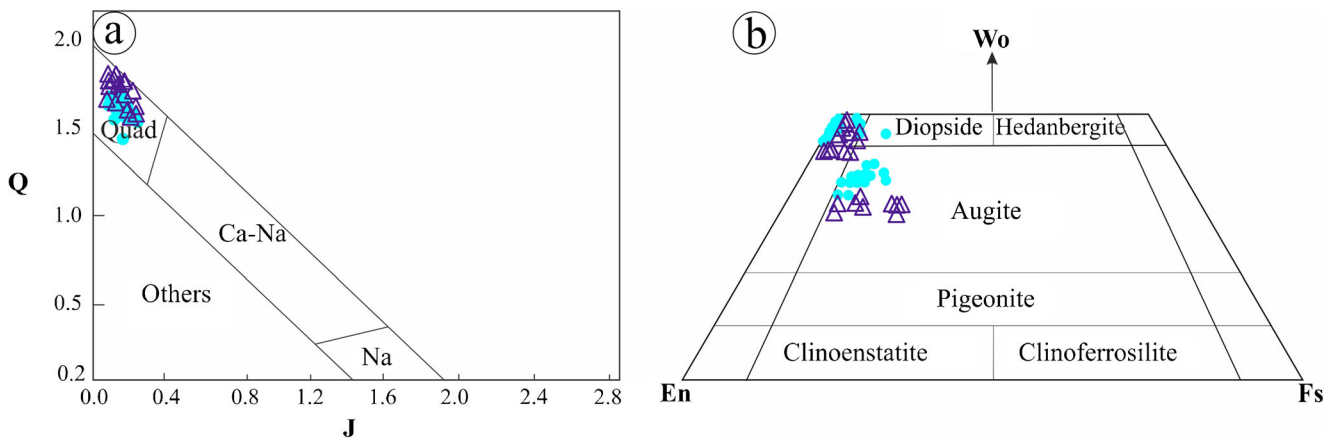
Fig. 6 a Classification of clinopyroxene from the Andarian volcanic rocks in Q–J diagram (J = 2Na, Q = Ca + Mg + Fe^{2+}) (Morimoto 1988). **b** Clinopyroxenes classification in wollastonite (Wo)-ferrosilite (Fs)-enstatite (En) diagram (Morimoto 1988). Symbols as in Fig. 4

Table 5 Chemical compositions and calculated mineral formulae of the biotites from the Andarian volcanic rocks (*H.A* hornblende andesite, *B.A* basaltic andesite)

| Sample number	An-41-10-1	AN-41-11-2	AN-41-12	AN-41-13	AN-41-14	AN-41-15	AN-43-16	AN-43-17	AN-43-18	An-44-28	An-44-28-2	An-44-28-3	An-49-12	An-49-12-2
	H.A	H.A	H.A	H.A	H.A	H.A	H.A	H.A	H.A	B.A	B.A	B.A	B.A	B.A
SiO_2	33.65	35.67	32.29	34.45	34.54	35.59	35.42	36.01	35.17	37.40	37.72	37.71	36.12	36.93
TiO_2	3.27	2.70	0.49	0.68	0.63	0.74	1.22	1.28	1.17	4.50	4.77	4.87	4.55	4.31
Al_2O_3	14.32	14.96	17.77	16.69	17.90	16.93	16.30	16.14	16.57	13.42	13.53	13.27	12.97	13.44
Cr_2O_3	bdl	bdl	bdl	bdl	bdl	bdl	bdl	bdl	bdl	0.05	bdl	bdl	0.05	bdl
FeO*	12.31	11.96	11.78	11.90	11.29	11.72	11.55	11.09	11.69	8.92	7.92	8.52	11.86	9.84
MnO	0.10	0.13	0.15	0.11	0.15	0.16	0.10	0.15	0.15	2.71	2.20	2.23	0.67	1.85
MgO	16.51	17.58	16.71	18.61	17.34	18.01	17.80	17.78	17.86	20.21	20.95	20.17	17.29	17.97
CaO	4.27	0.53	0.72	0.78	0.21	0.52	0.60	0.43	0.49	bdl	bdl	bdl	0.71	0.15
Na_2O	0.48	0.48	0.40	0.29	0.75	0.45	0.56	0.49	0.36	1.34	1.09	1.06	0.89	0.69
K_2O	7.27	7.45	7.16	6.82	8.75	7.66	7.84	8.05	6.45	4.50	4.77	4.87	4.55	4.31
F	0.70	0.87	0.17	0.58	0.56	1.49	0.57	0.53	0.46	2.71	2.20	2.23	0.67	1.85
Cl	0.10	0.09	0.11	0.05	0.06	0.06	0.09	0.10	0.11	0.80	0.68	0.63	0.43	0.55
Total	92.98	92.42	87.75	90.96	92.18	93.33	92.05	92.05	90.48	96.56	95.83	95.56	90.76	91.89
Normalization based on 24 O														
Si	5.204	5.450	5.172	5.312	5.291	5.403	5.411	5.483	5.414	5.507	5.516	5.550	5.562	5.632
Ti	0.381	0.310	0.059	0.079	0.072	0.085	0.140	0.146	0.135	0.499	0.525	0.539	0.526	0.494
Al_{IV}	2.611	2.550	2.828	2.688	2.709	2.597	2.589	2.517	2.586	2.328	2.333	2.302	2.355	2.368
Al_{VI}	0.000	0.144	0.527	0.346	0.523	0.433	0.347	0.381	0.421	0.000	0.000	0.000	0.000	0.047
Cr	bdl	bdl	bdl	bdl	bdl	bdl	bdl	bdl	bdl	0.006	bdl	bdl	0.006	bdl
Fe_{total}	1.593	1.529	1.578	1.534	1.446	1.488	1.476	1.412	1.505	1.099	0.968	1.048	1.528	1.254
Mn	0.013	0.016	0.020	0.014	0.019	0.020	0.013	0.019	0.019	0.338	0.273	0.278	0.087	0.239
Mg	3.807	4.004	3.991	4.276	3.959	4.076	4.055	4.037	4.099	4.435	4.566	4.425	3.969	4.085
Ca	0.707	0.087	0.124	0.129	0.035	0.085	0.098	0.071	0.080	bdl	bdl	bdl	0.117	0.025
Na	0.143	0.143	0.124	0.087	0.223	0.132	0.165	0.144	0.107	0.383	0.310	0.303	0.267	0.205
K	1.435	1.452	1.462	1.342	1.709	1.483	1.528	1.563	1.266	0.845	0.890	0.915	0.893	0.838
F	0.341	0.421	0.088	0.283	0.273	0.717	0.275	0.257	0.224	1.263	1.017	1.039	0.325	0.891
Cl	0.026	0.023	0.029	0.013	0.017	0.016	0.023	0.026	0.028	0.200	0.169	0.158	0.113	0.143
Fe/Fe+Mg	0.295	0.276	0.283	0.264	0.268	0.267	0.267	0.259	0.269	0.199	0.175	0.191	0.278	0.235
Location	core	core	core	core	core	core	core	core	core	core	core	rim	core	rim
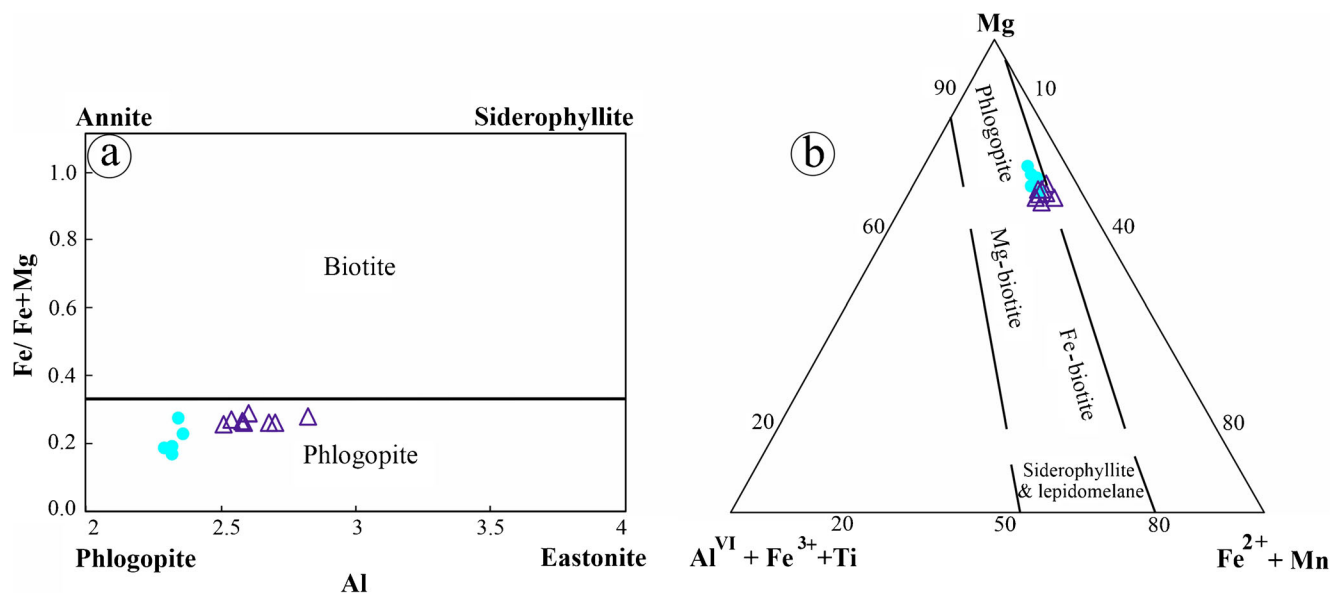
Fig. 7 Mineral chemistry of biotite in the Andarian volcanic rocks. **a** Al vs. Fe/(Fe+Mg) diagram showing the composition of biotite (Foster 1960). **b** Ternary diagram for biotite classification (Foster 1960). Symbols as in Fig. 4

move during hydrothermal alteration, making REE-related interpretation difficult. Therefore, we used only fresh samples for interpretation of chondrite-normalized REE and primitive mantle-normalized multi-element diagrams. For this reason, the rhyodacitic samples were not included. Chondrite-normalized REE patterns (McDonough and Sun 1995) of the Andarian volcanic rocks show general similar distribution patterns (Fig. 12a). In primitive mantle-normalized diagram (McDonough and Sun 1995), all of the Andarian volcanic samples display the enrichment in large ion lithophile elements (LILEs; e.g., Cs, Rb, Ba, and Sr), and depletion in high field strength elements (HFSE, e.g., Nb, Ta, and Ti) (Fig. 12b).

Discussion

Tectonic setting and magmatic series of the volcanic rocks

There is evidence that the formation of ore deposits in the AAMZ is related to a back-arc (e.g., Richards and Sholeh 2016) or a continental-arc setting (Calagari 2004; Hassanpour 2010; Alirezaei et al. 2015). However, a post-collisional setting is reported for plutonic and volcanic rocks in the AAMZ by previous studies (e.g., Dilek et al. 2010; Jamali et al. 2010; Maghsoudi et al. 2014; Moritz et al. 2016).
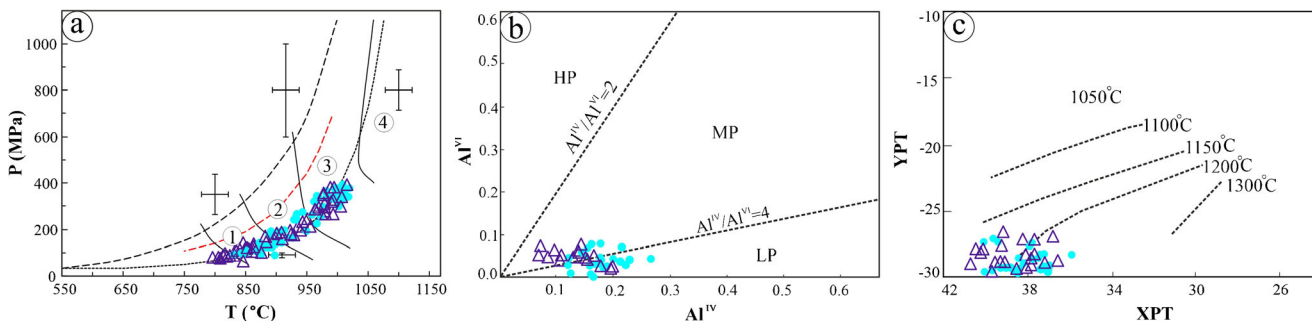
Fig. 8 a Distribution of the amphibole samples in T-P diagram (Ridolfi et al. 2010); (1) (Mg-Hbl + Pl ± Opx ± Mgn ± Ilm ± Bt), (2) (Tsc-Prg + Pl ± Cpx ± Opx ± Mgn ± Ilm), (3) (Tsc-Prg ± Pl ± Ol ± Cpx ± Opx ± Mgn ± Ilm), and (4) (Cpx ± Mgn ± Ol ± Pl). **b** Al^{IV} vs. Al^{VI} diagram of clinopyroxene samples (Aoki and Shiba 1973). **c** XPT vs. YPT diagram (Soesoo 1997) of clinopyroxene samples for the estimation of temperature. (XPT= 0.446 SiO_2 + 0.187 TiO_2 − 0.404 Al_2O_3 + 0.346 FeO − 0.052 MnO + 0.309 MgO + 0.431 CaO − 0.466 Na_2O and YPT= −0.369 SiO_2 + 0.535 TiO_2 − 0.317 Al_2O_3 + 0.323 FeO + 0.235 MnO − 0.516 MgO − 0.167 CaO − 0.153 Na_2O). Symbols as in Fig. 4

Table 6 Representative thermobarometry results of the Andarian volcanic rocks. (a) Amphibole-plagioclase thermometry (Holland and Blundy 1994), (b) Al-in-hornblende barometry (Anderson and Smith 1995), (c) Ti-in-hornblende thermometry (Otten 1984), (d) Al [VI]-in-hornblende barometry (Larocque and Canil 2010)

Hornblende andesite

Sample number	AN-40-1-2	AN-40-1-2	AN-40-8	AN-40-8-3	AN-40-8-2	An-40-10	AN-40-10-3	AN-43-10-1	AN-43-11	AN-50-24-3	AN-50-22	AN-72-3 av	AN-72-12	AN-72-23-2	AN-72-21-1	AN-41-2-3	AN-41-9-2
[a]T (°C)	844	850	837	811	846	860	855	892	865	780	809	744	775	808	710	760	834
[b]P (kb)	1.02	0.82	1.66	2.21	1.35	2.11	2.06	1.04	1.98	1.01	1.59	2.08	1.96	1.25	2.08	2.80	2.94

Basaltic andesite

Sample number	AN-42-2-1	AN-42-11-1	AN-44-1-3	AN-44-3-1	AN-40-8	AN-44-10-1	AN-44-22-1	AN-46-1-1	AN-48-7-1	AN-48-7-1	AN-48-18-2	AN-48-27-2	AN-48-25-2	AN-49-1-2	AN-49-8-2	AN-49-15-1
[a]T (°C)	843	764	884	892	837	880	864	739	799	774	827	880	784	795	707	871
[b]P (kb)	2.47	2.73	0.80	1.02	1.66	1.00	1.16	2.84	2.30	1.66	0.93	1.49	1.63	1.28	1.79	1.71

Hornblende andesite

Sample number	An-40-10	AN-41-2	AN-41-6	AN-41-3	AN-41-2-2	AN-41-3	AN-43-11	AN-50-2	AN-50-8	AN-50-13	AN-50-22-3	AN-50-23	AN-50-23-2	AN-72-20	AN-40-2	AN-49-1	AN-50-9
[c]T (°C)	897	830	924	906	854	921	943	911	906	837	799	783	796	773	916	899	776
[d]P (kb)	1.11	2.48	1.83	0.90	1.09	3.43	1.17	2.19	1.51	1.03	1.26	1.18	2.29	0.74	0.66	0.49	0.57

Basaltic andesite

Sample number	AN-42-2-2	AN-42-6	AN-42-7	AN-44-1	AN-44-1-2	AN-4-6-1	AN-46-2	AN-46-13-3	AN-42-11	AN-42-19	AN-46-14-2	AN-48-1	AN-44-1	AN-48-1	AN-46-13-2	AN-48-7	AN-49-14	AN-49-15
[c]T (°C)	948	954	942	860	927	810	781	781	792	943	924	881	860	860	774	839	946	846
[d]P (kb)	0.98	2.41	1.43	0.65	0.43	1.93	2.72	1.47	2.27	2.94	3.51	1.06	0.65	0.65	1.58	1.53	0.44	0.95
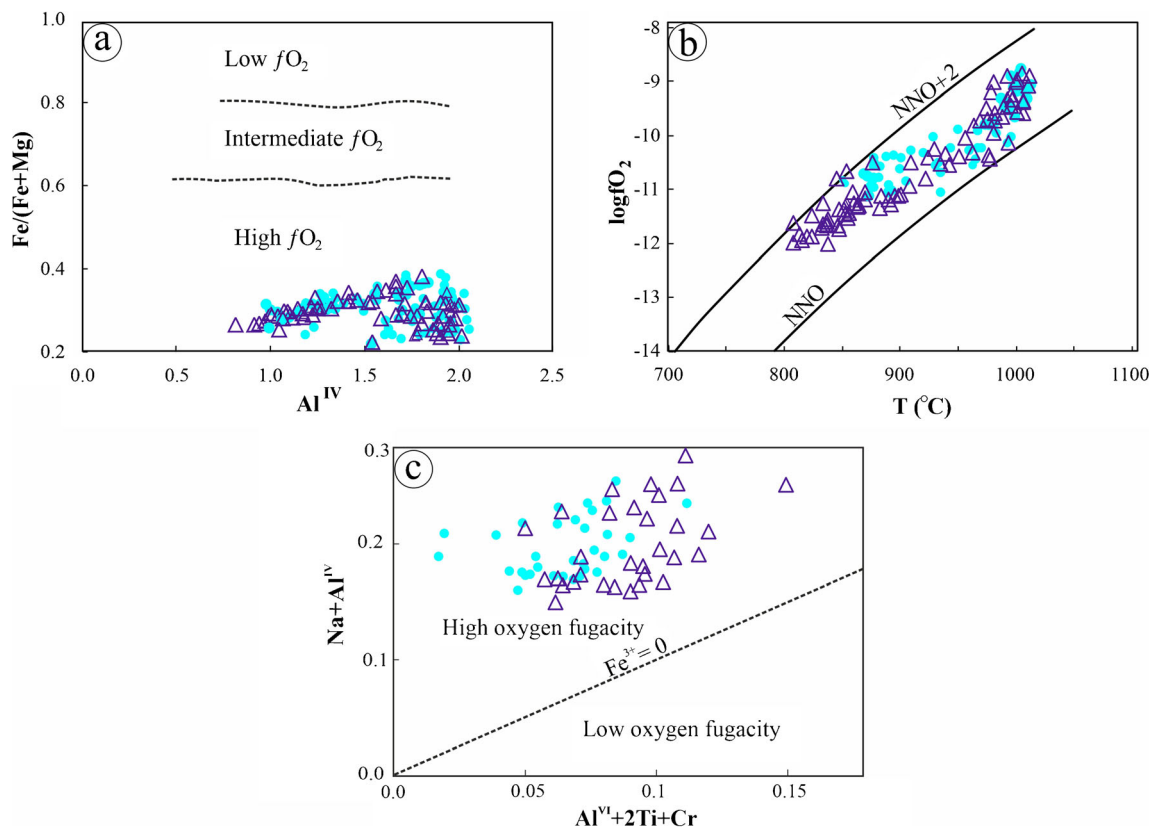
Fig. 9 Oxygen fugacity estimation of the Andarian volcanic rocks. **a** Binary Al^{IV} vs. (Fe/Fe + Mg) plot for amphibole (Anderson and Smith 1995). **b** T (^{0}C) vs. log fO_2 diagram for amphibole (Ridolfi et al. 2010). **c** Na+Al^{IV} vs. Al^{VI}+2Ti+Cr diagram for Clinopyroxene (Schweitzer et al. 1979). Symbols as in Fig. 4

In order to discrimination different tectonic settings, various diagrams are used based on the whole rock chemistry of the volcanic rocks. In the TiO_2/100–La–Ce/P_2O_5 ternary diagram, the Andarian volcanic samples plot in the overlapping continental and post-collisional arc fields (Fig. 13a). Moreover, two other diagrams, including Zr–Y and Al_2O_3–TiO_2 diagrams (Fig. 13b, c), confirm an arc-related setting for the studied samples. Additionally, the Zr*3–Nb*50–Ce/P_2O_5 plot (Müller and Groves 1997) which allows to distinguish continental and post-collisional arcs, suggests the post-collisional arc setting (Fig. 13d). More evidences for such

setting are connected to the trace element and REE patterns of the Andarian volcanic rocks (e.g., the LILE enrichments and Nb, Ta, and Ti depletions). In fact, these results are consistent with the patterns of magmas generated in other post-collisional settings specifically with the Miocene–Quaternary volcanic sequences in the Lesser Caucasus (Dilek et al. 2010). The evaluation of post-collisional setting for the studied volcanic rocks is also compatible with a possible timing of continental collision events in the region. The age of initial collision between the Arabia-Eurasian plates is possibly related to Eocene (Allen and Armstrong 2008; Kheirkhah et al. 2009;

Fig. 10 Discrimination diagrams to distinguish magma source for the Andarian volcanic rocks. **a** Al_2O_3 vs. TiO_2 diagram for amphibole (Changyi and Sanyuan 1984). **b** MgO vs. FeO*/(FeO* + MgO) diagram for biotite (Zhou 1986). Symbols as in Fig. 4
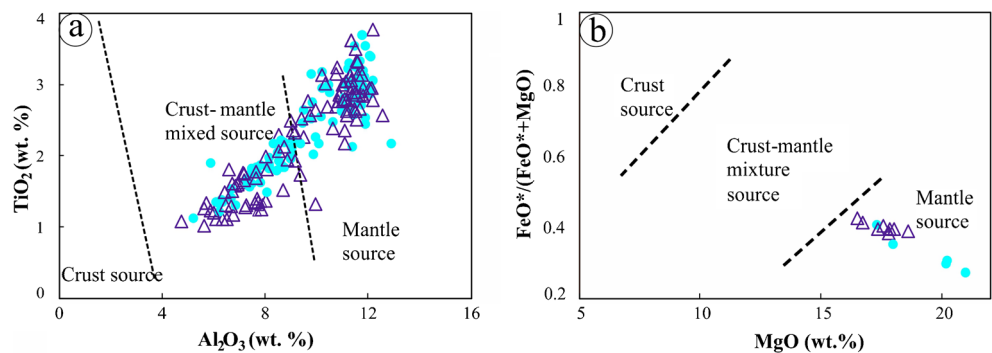
Table 7 Major oxides (wt%), trace elements, and rare earth elements (ppm) analysis of the Andarian volcanic rocks (*A* andesite, *R* rhyodacite)

Sample number	AN-38	AN-39	AN-43	AN-48	AN-49	MAN-55	AN-101	AN-U-93
	A	**A**	**A**	**A**	**A**	**A**	**R**	**R**
SiO_2	63.81	62.76	60.88	62.96	62.59	65.05	70.75	65.55
TiO_2	0.73	0.80	0.84	0.75	0.77	0.66	0.43	0.61
Al_2O_3	16.58	15.12	15.43	15.64	15.55	16.17	15.71	15.73
Fe_2O_3*	3.50	4.81	5.06	4.66	4.82	4.43	2.13	3.91
MnO	0.10	0.06	0.08	0.07	0.08	0.03	0.01	0.07
MgO	1.67	3.60	3.86	3.58	3.59	2.92	1.56	1.75
CaO	6.86	5.01	5.76	4.77	4.95	3.24	1.19	3.26
Na_2O	4.67	5.00	5.17	4.91	4.92	5.20	5.19	4.50
K_2O	1.77	2.41	2.45	2.19	2.27	1.87	2.88	4.35
P_2O_5	0.29	0.44	0.48	0.40	0.40	0.34	0.12	0.28
Total	99.97	100.02	100.01	99.94	99.94	99.90	99.99	100.01
Ba	667	896	953	794	816	645	546	569
Rb	24.06	34.49	47.41	43.40	45.91	52	75	133
Sr	671	938	1022	836	819	639	338	570
Zr	125	174	174	150	157	135	88.25	199
Nb	10.05	23.10	23.96	18.73	18.96	16.02	7.62	40
Cd	1.97	bdl	4.61	1.14	bdl	1.35	15.97	bdl
Cs	0.405	0.907	2.203	0.955	1.251	1.983	5.1	2.239
La	26.53	39.57	41.37	34.97	35.67	26.14	12.38	59.31
Ce	43.05	66.63	70.26	58.85	60.18	46.62	21.10	94.54
Pr	5.23	7.41	7.95	6.53	6.85	5.19	2.890	9.96
Nd	20.07	27.75	29.10	24.55	25.53	18.48	9.32	33.04
Sm	3.39	4.27	4.22	3.85	4.16	3.42	2.06	5.43
Eu	1.00	1.34	1.36	1.19	1.19	0.906	1.01	1.11
Gd	3.29	3.36	3.36	2.93	3.48	2.24	1.86	4.33
Tb	0.418	0.369	0.411	0.326	0.330	0.291	0.475	0.522
Dy	1.99	2.07	2.05	1.97	1.69	1.77	1.28	3.06
Ho	0.373	0.372	0.386	0.335	0.350	0.303	0.420	0.528
Er	1.47	0.979	0.906	0.942	1.05	0.911	0.664	1.643
Tm	0.185	0.113	0.160	0.104	0.148	0.136	0.368	0.240
Yb	0.944	0.805	0.979	0.855	0.836	0.778	0.894	1.563
Lu	0.233	0.147	0.197	0.146	0.142	0.127	0.192	0.187
Y	12.20	10.37	11.07	9.42	10.07	8.43	5.36	15.15
Hf	2.93	3.76	3.92	3.22	3.74	2.70	2.65	6.01
Ta	0.514	1.16	1.27	0.95	1.00	1.50	0.715	2.90
Pb	6.02	9.9	10.7	8.30	10.6	4.48	21.9	12.0
Th	6.06	11.99	11.74	9.33	10.04	7.03	4.75	46
U	1.45	2.65	2.66	2.22	2.35	1.89	1.65	5.09
Sc	20.69	18.40	18.55	17.90	17.80	18.47	16.90	19.20
V	97.87	94.75	96.38	96.96	99.54	93.70	57.10	77.10
Cr	70.41	110	110	97	110	77.15	37.63	30.81
Co	10.9	14.6	15.8	13.9	13.7	192	5.79	8.63
Ni	42.53	53	69	55	76	61	21.66	26.69
Zn	36.89	54	58	53	61	29.33	42	36.42

Dilek et al. 2010; Jamali et al. 2010; Sokol et al. 2018; Rabiee et al. 2020). However, the time of collision is still controversial.

Several discrimination diagrams have been used for tracing the magma affinity in the Andarian area. Zr/Y vs. Th-Yb graph (Ross and Bédard 2009) shows that all the volcanic rock
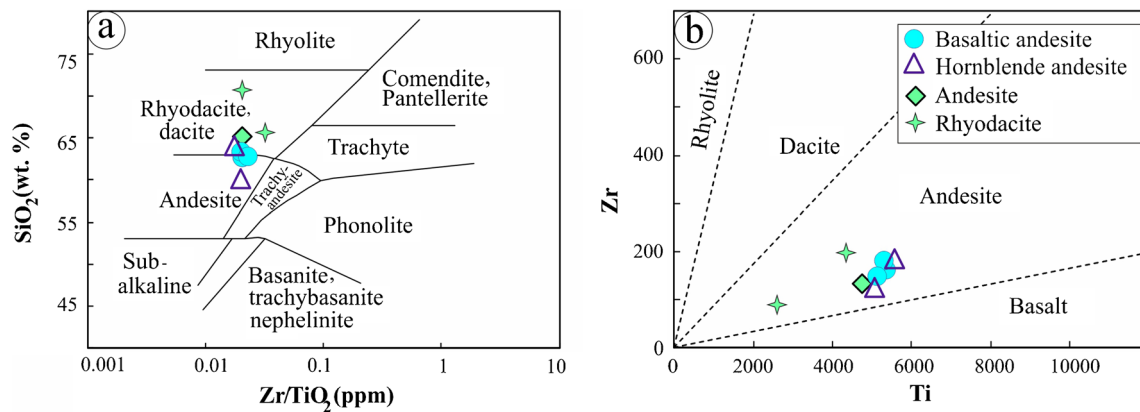
Fig. 11 Geochemical classification of the Andarian volcanic rocks. **a** Zr/TiO$_2$ vs. SiO$_2$ (Winchester and Floyd 1977). **b** Ti–Zr diagram (Hallberg 1984)

samples belong to the calc-alkaline domain (Fig. 14a). The AFM diagram of Fig. 14b (Irvine and Baragar 1971), which discriminate tholeiitic and calc-alkaline series, indicates a calc-alkaline affinity for the analyzed samples. The Zr vs. Y (Fig. 14c) binary diagram (Barrett and MacLean 1999) confirms the calc-alkaline nature of the studied samples. Furthermore, the calc-alkaline nature correlates with the mineral chemistry results such as biotite, amphibole, and clinopyroxene.

The chemical composition of biotite/phlogopite reflects the chemical composition of the rocks, providing that the mica is a primary magmatic mineral. Only in this case biotite/phlogopite provides reliable information. The Al^{VI} contents range from 0.0 to 0.52 apfu indicating a magmatic origin for the analyzed biotites/phlogopites (e.g., Nachit et al. 2005; Tavakoli et al. 2019, Table 5). Accordingly, the oxides of Al, Mg, and Fe content of the biotites from the Andarian volcanic rocks indicate calc-alkaline nature (Fig. 14d). Moreover, this result has been confirmed by the chemistry of clinopyroxenes and amphiboles. Clinopyroxenes of both rock types, with a wide range in Al$_2$O$_3$ content (0.60–5.99%), fall into the calc-alkaline field (after Le Bas 1962; Fig. 14e). According to Molina et al.'s (2009), amphiboles from sub-alkaline melts have typically lower Al$_2$O$_3$ and

TiO$_2$ content. As can be observed in Fig. 14 f, most of the studied points plot in the sub-alkaline domain. These findings have also been certified by the range of oxygen fugacity in the samples. Since ΔNNO values of the amphiboles in the studied volcanic rocks (0.10<ΔNNO<2.16) correlate to normal calc-alkaline values (−1<ΔNNO<+2.7), it confirms that the samples were derived from calc-alkaline (arc-related) magma (Carmichael 1991; Behrens and Gaillard 2006; Ridolfi et al. 2010).

P–T conditions

The composition of magmatic plagioclase depends on different physical parameters such as temperature, total pressure, and the water content of the melt (e.g., Ustunisik et al. 2014; Bennett et al. 2019; Yang et al. 2019; Cao et al. 2019; Jamshidibadr et al. 2020). Zoning structures in plagioclases provide an opportunity to identify the dynamics and changes of the magma during its evolution. On the other hand, different zoning patterns in plagioclase phenocrysts can record the chemical relationships between melt composition and crystal growth.

As mentioned in the previous section, the studied phenocrysts show micro-scale oscillatory zoning with rather coarse
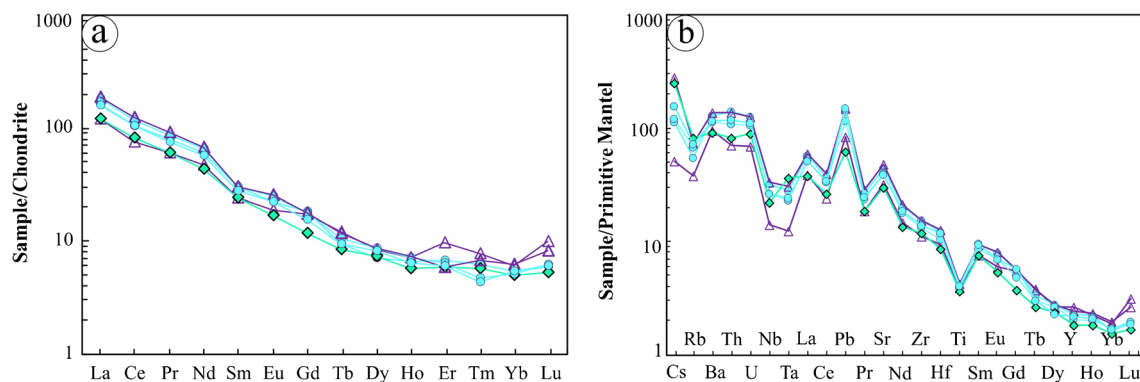
Fig. 12 **a** Chondrite-normalized rare earth element (REE) pattern of the Andarian volcanic rocks (McDonough and Sun 1995). **b** Primitive mantle-normalized multi-element diagrams (McDonough and Sun 1995)
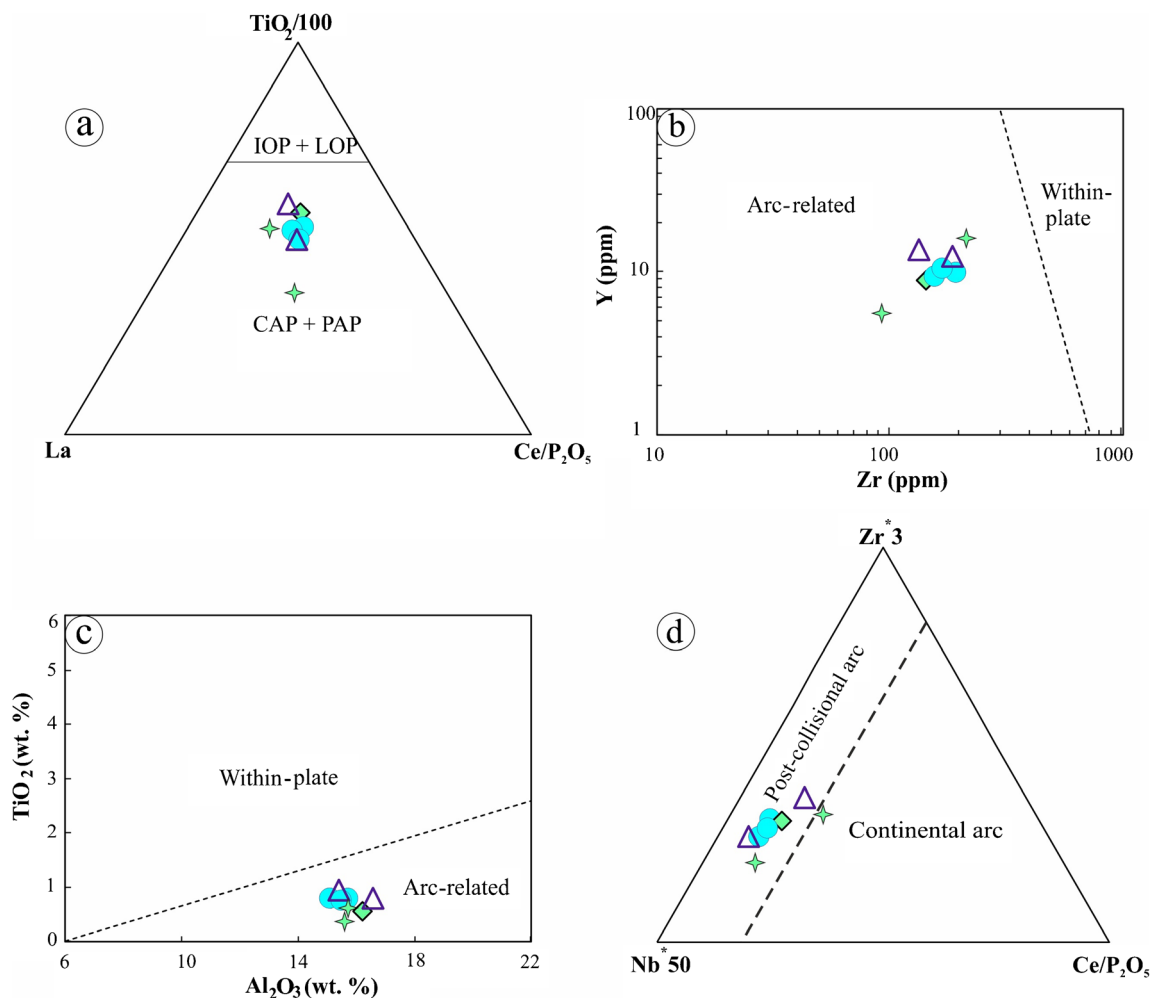
Fig. 13 Tectonic discrimination diagrams for the Andarian volcanic rocks. **a** $TiO_2/100$, La, and Ce/P_2O_5 diagram (Müller and Groves 1997). **b**, **c** Zr vs. Y diagram and Al_2O_3–TiO_2 graph (Müller and Groves1997). **d** $Zr*3$–$Nb*50$–Ce/P_2O_5 plot (Müller and Groves 1997).

CAP: continental arcs; PAP: post-collisional arc; IOP: initial oceanic rocks; LOP: late oceanic arcs; WIP: within-plate settings. Symbols as in Fig. 11

oscillations (>10 µm) and the ΔAn amplitude of 4 mol% (0.5 to 6.8 mol%) in both the core and rim. Supposing the same crystallization sequence for amphibole and plagioclase, estimation of the plagioclase formation state will be possible by using amphibole thermobarometry (Cao et al. 2019). Plagioclase in a large magma chamber can produce fluctuations of An contents at a rate of ~3% An per kbar (Ustunisik et al. 2014). Therefore, the wide range of ΔAn (0.5 to 6.8 mol%) in the oscillatory zoning of plagioclase suggests relatively unstable pressure conditions in the magma chamber during plagioclase crystallization. These results are consistent with the wide variations in the pressure values recorded by the amphibole geobarometer (0.5–2.9 kbar). Development of oscillatory zoning with coarse oscillations in plagioclase is interpreted either as magma mixing (e.g., Streck 2008; Neave et al. 2013; Velasco Tapia et al. 2013; Lai et al. 2016) or changes in the physiochemical parameters in a magma chamber (Yang et al. 2019). The wide range of variations

in the physicochemical parameters (P = 0.5–2.9 kbar, T = 707–899°C, water-rich, fO_2 = 0.10<ΔNNO<2.16) is confirmed by amphibole chemistry. Considering the same crystallization conditions for amphibole and plagioclase, oscillatory zoning in plagioclase was probably controlled by changes in the physicochemical conditions rather than magma mixing.

Additional support for variable physicochemical conditions (i.e., P, T, fO_2, and water activity) comes from the compositional diversity in the studied amphiboles that varies from edenite to tschermakite (Scaillet and Evans 1999; Grove et al. 2003; Rooney et al. 2011; Lisboa et al. 2020). The thermobarometric data reveal that the calculated values for the Andarian volcanic rocks are more variable than the expected values. The wide range of pressure (0.5–2.9 kbar for the amphiboles) demonstrates that the magma probably crystallized at a large depth range.

Furthermore, pressure conditions of a number of phenocrysts have been evaluated from crystal core to the rim
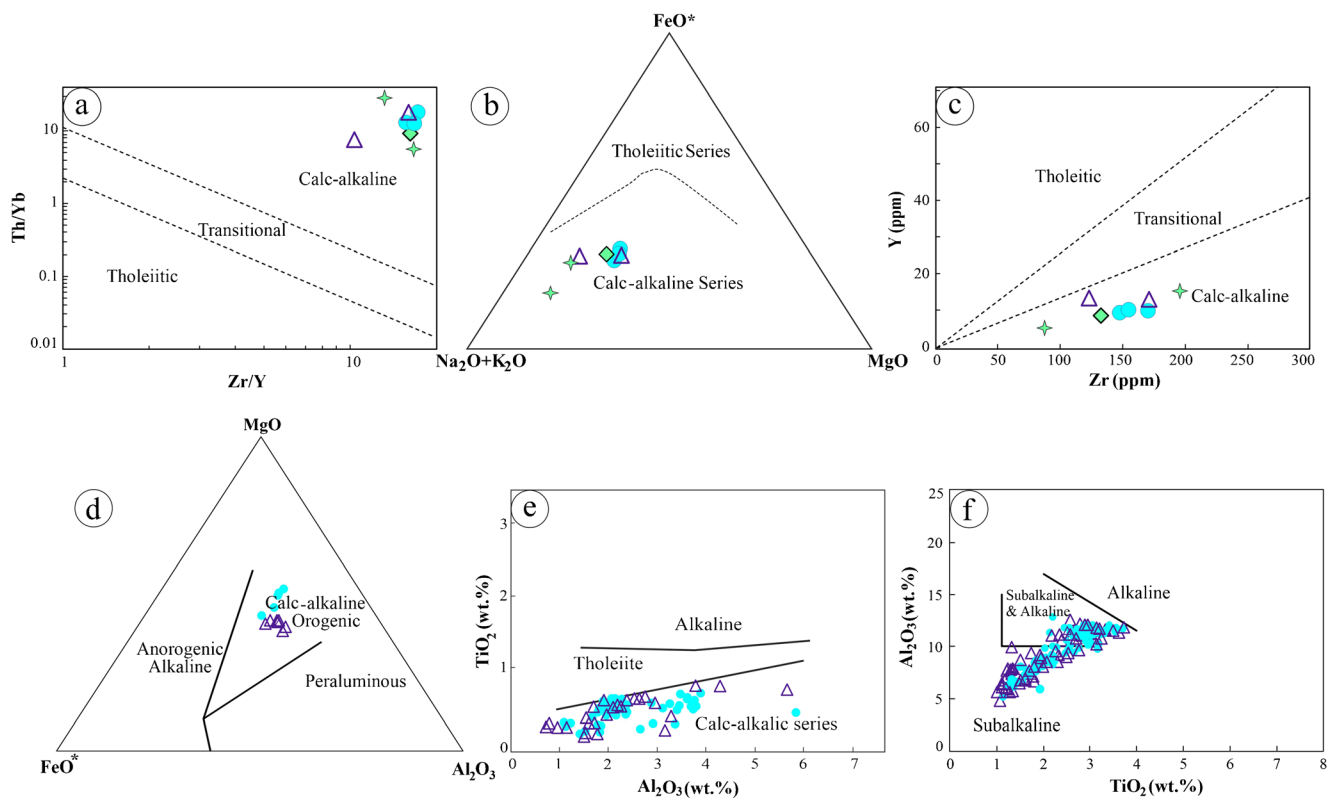
Fig. 14 The magmatic affinity of discriminant diagrams for the Andarian volcanic rocks. **a** Zr/Y vs. Th-Yb diagram (Ross and Bédard 2009). **b** AFM (A=Na₂O+K₂O, F=FeO*, and M=MgO) diagram (Irvine and Baragar 1971). **c** Zr vs. Y diagram (Barrett and MacLean 1999). **d**

Discrimination diagram to distinguish magma series for the Andarian volcanic rocks for biotite (Abdel-Rahman 1994). **e** Al₂O₃ vs. TiO₂ diagram for clinopyroxene (after Le Bas 1962). **f** Amphiboles in the TiO₂ vs. Al₂O₃ diagram (Molina et al. 2009). Symbols as in Fig. 11

(Table 3). The results show an irregular variation in the patterns of temperature but a decrease in the pressure from core to rim. An increasing SiO₂, chemical compositional changes, and decreasing calculated temperature and pressure in the amphiboles from core to rim are attributed to a normal zoning (Walker et al. 2013; Erdmann et al. 2014). In spite of the changes in the crystallization pressures and temperatures, the chemical composition of most amphibole phenocrysts with the exception of a few phenocrysts (these phenocrysts have edenite cores with rims approaching hastingsite) remains unchanged from core to rim. Therefore, the rim-ward decreasing pressure cannot be explained by the likely presence of compositional zoning. Therefore, this suggests that the changes in crystallization pressure and temperature in the Andarian volcanic rocks are probably due to the role of relatively unstable pressure and temperature in the magma chamber recorded by the composition of plagioclase, amphibole, and clinopyroxene.

Magma nature

Chondrite-normalized REE patterns (McDonough and Sun 1995) of the Andarian volcanic rocks (Fig. 12a) are characterized by steep, LREE-enriched patterns (La$_N$/Yb$_N$~19-33;

Rollinson 1993; Bea 2015) with no significant Eu anomalies (Eu/Eu*= 0.91–1.10; Taylor and McLennan 1985), implying the possible presence of residual garnet in the magma source (Gill 2010). In contrast, the concaved-shaped HREE pattern, as well as higher values of Lu$_N$ (5.14–9.47) and Er$_N$ (5.66–9.21) than Yb$_N$ (4.84–6.07) and Tm$_N$ (4.22–7.47) values in the studied samples, probably reflects amphibole crystallization (Davidson et al. 2007; Bea 2015). Moreover, the Sm/Yb ratio is an indicator for constraining the mantle source mineralogy (Shaw 1970; Aldanmaz et al. 2000; Li and Chen 2014). Sm/Yb ratios between 2–4 and greater than 4 are assumed as residual amphibole and garnet in magma source, respectively (e.g., Kay et al. 1999; Kay et al. 2010). The garnet presence in magma source as a residual phase is inconsistent with estimated pressures for the studied volcanic rocks. Instead, amphibole appears to be more likely as a residual mineral regarding the estimated pressure as calculated by amphiboles chemistry (0.5 to 2.9 kbar) for the Andarian volcanic rocks. Oxygen fugacity and water pressure are the factors that can influence Eu anomaly (Kay et al. 2010). The absence of Eu anomalies in the Andarian volcanic samples may be due to a high oxygen fugacity in the magma source (Wilson 1989; Rollinson 1993). This feature is compatible with a high fugacity of magma that result from the amphibole and clinopyroxene chemistry in the

previous section. In primitive mantle-normalized diagram (McDonough and Sun 1995), all of the Andarian volcanic samples display the LILE enrichments (e.g., Cs, Rb, Ba, and Sr) and HFSE depletions (e.g., Nb, Ta, and Ti) (Fig. 12b). The results obtained in this section correspond well to the result reported for the Mivehrood pluton (Fig. 2) adjacent to the Andarian volcanic rocks (Alirezaei et al. 2015) that suggest they may have co-magmatic origin. Furthermore, as described by Ghorbani (2021), all rock types associated with the second to fourth magmatic episodes in the AAMZ are co-magmatic (based on petrographic descriptions together with geochemical data). In terms of mineral chemistry and petrology, the petrogenetic relationship between the Andarian hornblende and basaltic andesite rocks is close that suggests co-magmatic nature for the volcanic rocks. In addition, the similar normalized trace element and REE patterns in both rock types support the co-magmatic origin for them.

Conclusion

The magmatism in AAMZ evolved in five main episodes from Upper Cretaceous to Quaternary. The studied volcanic rocks are representative of the fourth magmatic episode in the Andarian region, northwest Iran. Based on the petrology, mineral chemistry, and bulk rock geochemistry data from the Andarian volcanic rocks, the following conclusions were obtained:

1. The Andarian volcanic rocks include basaltic andesite, andesite, hornblende andesite, dacite, and rhyodacite showing a range from 60.88 to 70.75 wt% in SiO_2. The Neogene (possibly Pliocene, based on stratigraphic field relations) Andarian volcanic rocks mainly consist of hornblende and basaltic andesite. Despite their lithological differences, these rocks share broad similarities in mineral chemistry, thermobarometric data, and geochemistry, indicating co-magmatic origin.
2. The Andarian volcanic rocks display LILE enrichments, HFSE depletions, and strong LREE-enrichment with no Eu anomalies, similar to that of post-Miocene volcanic sequences in other parts of AAMZ and the Lesser Caucasus.
3. Considering mineral chemistry, amphibole, and plagioclase, the Andarian volcanic rocks were crystallized at high oxygen fugacity conditions (Log fO_2 = −8.8 to −12 bars) and at temperatures ranging from 707 to 899°C and pressures ranging from 0.5 to 2.9 kbar. Therefore, the wide range of pressure, temperature, and oxygen fugacity, as well as oscillatory zoning in plagioclase, demonstrates that physiochemical conditions are possibly unstable in the magma chamber.
4. The bulk rocks' geochemistry and mineral compositions (biotite, amphibole, and clinopyroxene) clarify that the Neogene Andarian volcanic rocks are derived from an arc-related calc-alkaline magma in a post-collisional setting. Therefore, the magma nature and tectonic setting perfectly correlate the published data in the AAMZ and occurrences in the Lesser Caucasus.

Data availability Representative data are available in the manuscript.

Declarations

Competing interests The authors declare that they have no competing interests.

References

Abdel-Rahman AFM (1994) Nature of biotites from alkaline, calc-alkaline, and peraluminous magmas. J Petrol 35:525–541

Akbarpur A (2007) Economic geology of the Kiamaki area, eastern Azerbaijan, with spatial view on Cu–Au mineralization in Masjed-Daghi. Dissertation, Free University of Iran.

Aldanmaz ERCAN, Pearce JA, Thirlwall MF, Mitchell JG (2000) Petrogenetic evolution of late Cenozoic, post-collision volcanism in western Anatolia, Turkey. J Volcanol Geotherm Res 102:67–95. https://doi.org/10.1016/S0377-0273(00)00182-7

Allen MB, Armstrong HA (2008) Arabia-Eurasia collision and the forcing of mid-Cenozoic global cooling. Palaeogeogr Palaeoclimatol Palaeoecol 265:52–58. https://doi.org/10.1016/j.palaeo.2008.04.021

Anderson JL, Smith DR (1995) The effects of temperature and f O_2 on the Al-in-hornblende barometer. Am Mineral 80:549–559. https://doi.org/10.2138/am-1995-5-614

Aoki KI, Shiba I (1973) Pyroxenes from lherzolite inclusions of Itinomegata, Japan. Lithos 6:41–51. https://doi.org/10.1016/0024-4937(73)90078-9

Aghazadeh M, Castro A Badrzadeh Z (2012) U–Pb age dating of Cenozoic plutonism in the Arasbaran magmatic zone, NW Iran. In 34th International Geological Congress, Brisbane, Australia.

Aghazadeh M, Castro A, Omran NR, Emami MH, Moinvaziri H, Badrzadeh Z (2010) The gabbro (shoshonitic)–monzonite–granodiorite association of Khankandi pluton, Alborz Mountains, NW Iran. J Asian Earth Sci 38:199–219. https://doi.org/10.1016/jjseaes201001002

Alirezaei S, Einali M, Jones P, Hassanpour S, Arjmandzadeh R (2015) Mineralogy, geochemistry, and evolution of the Mivehrood skarn and the associated pluton, northwest Iran. Int J Earth Sci 105:849–868. https://doi.org/10.1007/s00531-015-1200-4

Avagyan A, Sosson M, Philip H, Karakhanian A, Rolland Y, Melkonyan R, Rebaï S, Davtyan V (2005) Neogene to Quaternary stress field evolution in Lesser Caucasus and adjacent regions using fault kinematics analysis and volcanic cluster data. Geodin Acta 18:401–416

Avagyan A, Sosson M, Sahakyan L, Sheremet Y, Vardanyan S, Martirosyan M, Muller C (2018) Tectonic evolution of the Northern margin of the Cenozoic Ararat basin, Lesser Caucasus, Armenia. J Pet Geol 41:495–511. https://doi.org/10.1111/jpg12718

Barrett TJ, MacLean WH (1999) Volcanic sequences, lithogeochemistry, and hydrothermal alteration in some bimodal volcanic-associated massive sulfide systems. Rev Econ Geol 8:101–131. https://doi.org/10.5382/Rev0805

Bea F (2015) Geochemistry of the Lanthanide Elements. Reunión de la Sociedad Española de Mineralogía:1–12

Behrens H, Gaillard F (2006) Geochemical aspects of melts: volatiles and redox behavior. Elements 2:275–280. https://doi.org/10.2113/gselements25275

Bennett EN, Lissenberg CJ, Cashman KV (2019) The significance of plagioclase textures in mid-ocean ridge basalt (Gakkel Ridge, Arctic Ocean). Contrib Mineral Petrol 174:1–22. https://doi.org/10.1007/s00410-019-1587-1

Calagari AA (2004) Geology and fracture-related hypogene hydrothermal alteration and mineralization of porphyry copper deposit at Sungun. J Geol Soc India 64:595–618

Cao M, Evans NJ, Reddy SM, Fougerouse D, Hollings P, Saxey DW, McInnes BI, Cooke DR, McDonald BJ, Qin K (2019) Micro-and nano-scale textural and compositional zonation in plagioclase at the Black Mountain porphyry Cu deposit: implications for magmatic processes. Am Mineral 104:391–402

Castro A, Aghazadeh M, Badrzadeh Z, Chichorro M (2013) Late Eocene–Oligocene post-collisional monzonitic intrusions from the Alborz magmatic belt, NW Iran An example of monzonite magma generation from a metasomatized mantle source. Lithos 180:109–127. https://doi.org/10.1016/jlithos201308003

Carmichael IS (1991) The redox states of basic and silicic magmas: a reflection of their source regions? Contrib Mineral Petrol 106:129–141. https://doi.org/10.1007/BF00306429

Changyi J, Sanyuan A (1984) On chemical characteristics of calcic amphiboles from igneous rocks and their petrogenesis significance. J Mineral Petrol 3:1–9

Dabiri R, Emami M, Mollaei H, Chen B, Abedini M, Omran N, Ghaffari M (2011) Quaternary post-collision alkaline volcanism NW of Ahar (NW Iran): geochemical constraints of fractional crystallization process. Geol Carpath 62:547–562. https://doi.org/10.2478/v10096-011-0039-2

Davidson J, Turner S, Handley H, Macpherson C, Dosseto A (2007) Amphibole "sponge" in arc crust? Geol 35:787–790. https://doi.org/10.1130/G23637A1

Deer W, Howie RA, Zussman J (1992) An introduction to the rock-forming minerals, (Longman Scientific and Technical). London.

Dilek Y, Imamverdiyev N, Altunkaynak S (2010) Geochemistry and tectonics of Cenozoic volcanism in the Lesser Caucasus (Azerbaijan) and the peri-Arabian region: collision-induced mantle dynamics and its magmatic fingerprint. Int Geol Rev 52:536–578. https://doi.org/10.1080/00206810903360422

Dongen M, Weinberg RF, Tomkins AG (2010) REE-Y, Ti, and P remobilization in magmatic rocks by hydrothermal alteration during Cu-Au deposit formation. Econ Geol 105:763–776. https://doi.org/10.2113/gsecongeo1054763

Erdmann S, Martel C, Pichavant M, Kushnir A (2014) Amphibole as an archivist of magmatic crystallization conditions: problems, potential, and implications for inferring magma storage prior to the paroxysmal 2010 eruption of Mount Merapi, Indonesia. Contrib Mineral Petrol 167:1–23. https://doi.org/10.1007/s00410-014-1016-4

Ferdowsi R, Calagari A A, Hosseinzadeh M, Siahcheshm K (2015) The study of geochemistry, alteration, mineralization, fluid inclusions and genesis of base and precious metals (Cu, Au) in Astaraghan area, Kharvana, East-Azarbaijan. PhD thesis, Tabriz University, Iran (in Persian with English abstract).

Foster MD (1960) Interpretation of the composition of trioctahedral micas. U S Geol Surv 354:11–49. https://doi.org/10.3133/pp354B

Ghorbani M (2013) A summary of geology of Iran in the economic geology of Iran. Springer, Dordrecht https://www.springer.com/gp/book/9789400756243

Ghorbani M (2019) Lithostratigraphy of Iran. Springer. https://doi.org/10.1007/978-3-030-04963-8

Ghorbani M (2021) The geology of Iran: tectonic, magmatism and metamorphism. Springer. https://doi.org/10.1007/978-3-030-71109-2

Gill R (2010) Igneous rocks and processes: a practical guide. John Wiley & Sons. https://wwwwileycom/en-ir/Igneous Rocks and Processes, 9781444330656

Grove TL, Elkins-Tanton LT, Parman SW, Chatterjee N, Müntener O, Gaetani GA (2003) Fractional crystallization and mantle-melting controls on calc-alkaline differentiation trends. Contrib Mineral Petrol 145:515–533. https://doi.org/10.1007/s00410-003-0448-z

Hallberg JA (1984) A geochemical aid to igneous rock type identification in deeply weathered terrain. J Geochem Explor 20:1–8. https://doi.org/10.1016/0375-6742(84)90085-2

Hassanpour S, Alirezaei S, Selby D, Sergeev S (2015) SHRIMP zircon U–Pb and biotite and hornblende Ar–Ar geochronology of Sungun, Haftcheshmeh, Kighal, and Niaz porphyry Cu–Mo systems: evidence for an early Miocene porphyry-style mineralization in northwest Iran. Int J Earth Sci 104:45–59. https://doi.org/10.1007/s00531-014-1071-0

Hassanpour S (2013) The alteration, mineralogy and geochronology (SHRIMP U–Pb and ^{40}Ar/^{39}Ar) of copper-bearing Anjerd skarn, north of the Shayvar Mountain, NW Iran. Int J Earth Sci 102:687-699. https://doi.org/10.1007/s00531-012-0819-7

Hassanpour S (2010) Metallogeny and mineralization of copper and gold in Arasbaran Zone (Eastern Azerbaijan). PhD thesis, Shahid Beheshti University, Iran (in Persian with English abstract)

Hassanpour S (2017) The Sungun porphyry magma resource and the 120,000-year difference in age between the main stock and the first dike: New evidence from ^{87}Sr/^{86}Sr, ^{143}Nd/^{144}Nd and Pb, SHRIMP U–Pb zircon dating in NW Iran. Iran J Earth Sci 9:94–104

Hawthorne FC, Oberti R, Harlow GE, Maresch WV, Martin RF, Schumacher JC, Welch MD (2012) Nomenclature of the amphibole supergroup. Am Mineral 97:2031–2048. https://doi.org/10.2138/am.2012.4276

Hikov A (2011) Rare earth element mobility during hydrothermal alteration in Asarel porphyry copper deposit, Central Srednogorie. Comptes rendus de l'Academie bulgare des Sciences 64:1163–1170

Holland T, Blundy J (1994) Non-ideal interactions in calcic amphiboles and their bearing on amphibole-plagioclase thermometry. Contrib Mineral Petrol 116:433–447. https://doi.org/10.1007/BF00310910

Irvine TNJ, Baragar WRA (1971) A guide to the chemical classification of the common volcanic rocks. Can J Earth Sci 8:523–548. https://doi.org/10.1139/e71-055

Jamali H, Dilek Y, Daliran F, Yaghubpur A, Mehrabi B (2010) Metallogeny and tectonic evolution of the Cenozoic Ahar–Arasbaran volcanic belt, northern Iran. Int Geol Rev 52:608–630. https://doi.org/10.1080/00206810903416323

Jamali H, Mehrabi B (2015) Relationships between arc maturity and Cu–Mo–Au porphyry and related epithermal mineralization at the Cenozoic Arasbaran magmatic belt. Ore Geol Rev 65:487–501. https://doi.org/10.1016/joregeorev201406017

Jamshidibadr M, Tarabi S, Qolizadeh K (2020) Study of micro-textures and chemistry of feldspar minerals of East Sarbisheh volcanic complex (Eastern Iran), for evidence of magma chamber process. Iran J Earth Sci 12:10–31

Johnson MC, Rutherford MJ (1989) Experimental calibration of the aluminum-in-hornblende geobarometer with application to Long Valley caldera (California) volcanic rocks. Geol 17:837–841. https://doi.org/10.1130/0091-7613(1989)017

Kay SM, Coira BL, Caffe PJ, Chen CH (2010) Regional chemical diversity, crustal and mantle sources and evolution of central Andean Puna plateau ignimbrites. J Volcanol Geotherm Res 198:81–111. https://doi.org/10.1016/jjvolgeores201008013

Kay S M, Mpodozis C, Coira B (1999) Neogene magmatism, tectonism, and mineral deposits of the Central Andes (22 to 33 S latitude) In Geology and ore deposits of the Central Andes Lancaster, USA: Society of Economic Geologists, pp 27-59. https://doi.org/10.5382/SP0702

Kil Y, Jung H (2015) LA-ICP-MS analysis of natural rock samples using XRF glass beads. Geosci J 19:45–52. https://doi.org/10.1007/s12303-014-0063-1

Kheirkhah M, Allen MB, Emami M (2009) Quaternary syn-collision magmatism from the Iran/Turkey borderlands. J Volcanol Geotherm Res 182:1–12. https://doi.org/10.1016/jjvolgeores200901026

Lai Z, Zhao G, Han Z, Liu B, Bu X, Leng C (2016) Back-arc magma processes in the Okinawa Trough: new insights from textural and compositional variations of plagioclase in basalts. Geol J 51:346–356. https://doi.org/10.1002/gj2767

Larocque J, Canil D (2010) The role of amphibole in the evolution of arc magmas and crust: the case from the Jurassic bonanza arc section, Vancouver Island, Canada. Contrib Mineral Petrol 159:475–492. https://doi.org/10.1007/s00410-009-0436-z

Leake BE, Alan RW, William DB, Ernst AJB, Giovanni F, Jeol DJ, Frank CH, Hanan JK, Vladimir GK, John CS, Nicholas CNS, Eric JWW (2004) Nomenclature of amphiboles: additions and revisions to the international mineralogical associations amphibole nomenclature. Am Mineral 89:883–887. https://doi.org/10.1127/09351221/2004/0016-0191

Le Bas MJ (1962) The role of aluminum in igneous clinopyroxenes with relation to their parentage. Am J Sci 260:267–288. https://doi.org/10.2475/ajs2604267

Li Z, Chen B (2014) Geochronology and geochemistry of the Paleoproterozoic meta-basalts from the Jiao-Liao-Ji Belt, North China Craton: Implications for petrogenesis and tectonic setting. Precambrian Res 255:653–667. https://doi.org/10.1016/jprecamres201407003

Lisboa VAC, Conceição H, Rosa MLS, Marques GT, Lamarão CN, Lima ALR (2020) Amphibole crystallization conditions as record of interaction between ultrapotassic enclaves and monzonitic magmas in the Glória Norte Stock, South of Borborema Province. Braz J Geol 50(1-10):101590/2317–101590/4889202020190101

Maghsoudi A, Yazdi M, Mehrpartou M, Vosoughi M, Younesi S (2014) Porphyry Cu–Au mineralization in the Mirkuh Ali Mirza magmatic complex, NW Iran. J Asian Earth Sci 79:932–941. https://doi.org/10.1016/jjseaes201210002

Matossian AO, Baghdasaryan H, Avagyan A, Igityan H, Gevorgyan M, Havenith HB (2020) A new landslide inventory for the Armenian Lesser Caucasus: slope failure morphologies and seismotectonic influences on large landslides. Geosc 10:1–24. https://doi.org/10.3390/geosciences10030111

McDonough WF, Sun SS (1995) The composition of the Earth. Chem Geol 120:223–253. https://doi.org/10.1016/0009-2541(94)00140-4

Mehrpartou M (1997) Geological map of the Siahrood Quadrangle No 5267, 1:100000 Series. Geol Surv of Iran.

Molina JF, Scarrow JH, Montero PG, Bea F (2009) High-Ti amphibole as a petrogenetic indicator of magma chemistry: evidence for mildly alkalic-hybrid melts during evolution of Variscan basic–ultrabasic magmatism of Central Iberia. Contrib Mineral Petrol 158:69–98. https://doi.org/10.1007/s00410-008-0371-4

Morimoto N (1988) Nomenclature of pyroxenes. Mineral Petrol 39:55–76. https://doi.org/10.1016/jgca201209052

Moritz R, Johannes M, Maria O, Dave S, Massimo C, Nino P, Vladimir G, Ramaz M, Rafael M, Rodrig T, Arman V (2011) Major Cu, Au and Mo deposits of the Lesser Caucasus: products of diverse geodynamic settings. In 9th Swiss Geoscience Meeting Symposium, Zurich.

Moritz R, Rezeau H, Ovtcharova M, Tayan R, Melkonyan R, Hovakimyan S, Ramazanov V, Selby D, Ulianov A, Chiaradia M, Putlitz B (2016) Long-lived, stationary magmatism and pulsed porphyry systems during Tethyan subduction to post-collision evolution in the southernmost Lesser Caucasus, Armenia and Nakhitchevan. Gondwana Res 37:465–503. https://doi.org/10.1016/jgr201510009

Müller D, Groves DI (1997) Potassic igneous rocks and associated gold-copper mineralization. Springer, Berlin

Neave DA, Putirka KD (2017) A new clinopyroxene-liquid barometer, and implications for magma storage pressures under Icelandic rift zones. Am Mineral 102:777–794. https://doi.org/10.2138/am-2017-5968

Neave DA, Passmore E, Maclennan J, Fitton G, Thordarson T (2013) Crystal–melt relationships and the record of deep mixing and crystallization in the ad 1783 Laki Eruption, Iceland. J Petrol 54:1661–1690. https://doi.org/10.1093/petrology/egt027

Nachit H, Ibhi A, Ohoud MB (2005) Discrimination between primary magmatic biotites, reequilibrated biotites and neoformed biotites. Compt Rendus Geosci 337:1415–1420. https://doi.org/10.1016/jcrte200509002

Otten MT (1984) The origin of brown hornblende in the artfjallet gabbro and dolerites. Contrib Mineral Petrol 86:189–199. https://doi.org/10.1016/0024-4937(85)90033-7

Pazand K, Hezarkhani A (2018) Predictive Cu porphyry potential mapping using fuzzy modelling in Ahar–Arasbaran zone, Iran. Geol ecol landsc 2:229–239. https://doi.org/10.1080/2474950820181438741

Putirka KD (2008) Thermometers and barometers for volcanic systems. Rev Mineral Geochem 69:61–120. https://doi.org/10.2138/rmg2008693

Rabiee A, Rossetti F, Asahara Y, Azizi H, Lucci F, Lustrino M, Nozaem R (2020) Long-lived, Eocene-Miocene stationary magmatism in NW Iran along a transform plate boundary. Gondwana Res 85: 237–262. https://doi.org/10.1016/j.gr.2020.03.014

Rabiee A, Rossetti F, Tecce F, Asahara Y, Azizi H, Glodny J, Lucci F, Nozaem R, Opitz J, Selby D (2019) Multiphase magma intrusion, ore-enhancement and hydrothermal carbonatisation in the Siah-Kamar porphyry Mo deposit, Urumieh-Dokhtar magmatic zone, NW Iran. Ore Geol Rev 110. https://doi.org/10.1016/j.oregeorev.2019.05.016

Richards JP (2015) Tectonic, magmatic, and metallogenic evolution of the Tethyan orogen: from subduction to collision. Ore Geol Rev 70: 323–345. https://doi.org/10.1016/joregeorev201411009

Richards JP, Sholeh A (2016) The Tethyan tectonic history and Cu-Au metallogeny of Iran Tectonics and Metallogeny of the Tethyan Orogenic Belt. Society of Economic Geologists Special Publication 19:193–212

Ridolfi F, Renzulli A (2012) Calcic amphiboles in calc-alkaline and alkaline magmas: thermobarometric and chemometric empirical equations valid up to 1,130°C and 22 GPa. Contrib Mineral Petrol 163: 877–895. https://doi.org/10.1007/s00410-011-0704-6

Ridolfi F, Renzulli A, Puerini M (2010) Stability and chemical equilibrium of amphibole in calc-alkaline magmas: an overview, new thermobarometric formulations and application to subduction-related volcanoes. Contrib Mineral Petrol 160:45–66. https://doi.org/10.1007/s00410-009-0465-7

Rollinson H R (1993) Using geochemical data. Longman, Scientific & Technical, New York.

Rooney TO, Franceschi P, Hall CM (2011) Water-saturated magmas in the Panama Canal region: a precursor to adakite-like magma generation? Contrib Mineral Petrol 161:373–388. https://doi.org/10.1007/s00410-010-0537-8

Ross PS, Bédard JH (2009) Magmatic affinity of modern and ancient subalkaline volcanic rocks determined from trace-element

discriminant diagrams. Can J Earth Sci 46:823–839. https://doi.org/10.1139/E09-054

Saki A, Lucci F, Miri M, White JC (2021) Trondhjemite leucosomes generated by partial melting of a hornblende-gabbro (Alvand plutonic complex, Hamedan, NW Iran). Int Geol Rev 1:1–34. https://doi.org/10.1080/00206814.2020.1861554

Scaillet B, Evans BW (1999) The 15 June 1991 eruption of Mount Pinatubo I Phase equilibria and pre-eruption P–T–fO$_2$–f H$_2$O conditions of the dacite magma. J Petrol 40:381–411. https://doi.org/10.1093/petroj/403381

Schweitzer EL, Papike JJ, Bence AE (1979) Statistical analysis of clinopyroxenes from deep-sea basalts. Am Mineral 64:501–513

Shaw DM (1970) Trace element fractionation during anatexis. Geochim Cosmochim Acta 34:237–243. https://doi.org/10.1016/0016-7037(70)90009-8

Simmonds V, Moazzen M, Mathur R (2017) Constraining the timing of porphyry mineralization in northwest Iran in relation to Lesser Caucasus and Central Iran; Re–Os age data for Sungun porphyry Cu–Mo deposit. Int Geol Rev 59: 1561–1574. https://doi.org/10.1080/00206814.2017.1285258

Soesoo A (1997) A multivariate statistical analysis of clinopyroxene composition: empirical coordinates for the crystallisation PT-estimations. GFF 119:55–60. https://doi.org/10.1080/11035899709546454

Sokol K, Halama R, Meliksetian K, Savov IP, Navasardyan G, Sudo M (2018) Alkaline magmas in zones of continental convergence: the Tezhsar volcano-intrusive ring complex, Armenia. Lithos 320:172–191. https://doi.org/10.1016/j.lithos.2018.08.028

Soltanmohammadi A, Grégoire M, Rabinowicz M, Gerbault M, Ceuleneer G, Rahgoshay M, Bystricky M, Benoit M (2018) Transport of volatile-rich melt from the mantle transition zone via compaction pockets: implications for mantle metasomatism and the origin of alkaline lavas in the Turkish–Iranian plateau. J Petrol 59:2273–2310. https://doi.org/10.1093/petrology/egy097

Stocklin J (1968) Structural history and tectonics of Iran; a review. Am Assoc Pet Geol Bull 52:1229–1258. https://doi.org/10.1306/5D25C4A5-16C1-11D7-8645000102C1865D

Streck MJ (2008) Mineral textures and zoning as evidence for open system processes. Rev Mineral Geochem 69:595–622. https://doi.org/10.2138/rmg20086915

Tavakoli N, Davoudian AR, Shabanian N, Azizi H, Neubauer F, Asahara Y, Bernroider M (2019) Zircon U-Pb dating, mineralogy and geochemical characteristics of the gabbro and gabbro-diorite bodies, Boein–Miandasht, western Iran. Int Geol Rev:1–19. https://doi.org/10.1080/0020681420191583139

Taylor S R, McLennan S M (1985) The continental crust: its composition and evolution. United States.

Ustunisik G, Kilinc A, Nielsen RL (2014) New insights into the processes controlling compositional zoning in plagioclase. Lithos 200:80–93. https://doi.org/10.1016/jlithos201403021

Velasco Tapia F, Rodríguez Saavedra P, Marquez A, Navarro de León I, De Ignacio C, Marroquín Guerra SG, Quintanilla Garza J, Rangel Alvarez OM (2013) Mineralogical and geochemical evidence of magma mingling/mixing in the Sierra de las Cruces volcanic range, Mexican Volcanic Belt. J Iber Geol 39:147–166. https://doi.org/10.5209/rev_JIGE2013v39n141756

Vincent SJ, Allen MB, Ismail-Zadeh AD, Flecker R, Foland KA, Simmons MD (2005) Insights from the Talysh of Azerbaijan into the Paleogene evolution of the South Caspian region. Geol Soc Am Bull 117:1513–1533. https://doi.org/10.1130/B256901

Walker BA, Klemetti EW, Grunder AL, Dilles JH, Tepley FJ, Giles D (2013) Crystal reaming during the assembly, maturation, and waning of an eleven-million-year crustal magma cycle: thermobarometry of the Aucanquilcha Volcanic Cluster. Contrib Mineral Petrol 165:663–682. https://doi.org/10.1007/s00410-012-0829-2

Whitney DL, Evans BW (2010) Abbreviations for names of rock-forming minerals. Am Mineral 95:185–187. https://doi.org/10.2138/am20103371

Wilson M (1989) Igneous petrogenesis: a global tectonic approach. Chapman Hall, London

Winchester JA, Floyd PA (1977) Geochemical discrimination of different magma series and their differentiation products using immobile elements. Chem Geol 20:325–343. https://doi.org/10.1016/0009-2541(77)90057-2

Yang F, Huang XL, Xu YG, He PL (2019) Magmatic processes associated with oceanic crustal accretion at slow-spreading ridges: evidence from plagioclase in mid-ocean ridge basalts from the South China Sea. J Petrol 60:1135–1162. https://doi.org/10.1093/petrology/egz027

Zhiwei B, Zhenhua Z (2003) Rare-earth element mobility during ore-forming hydrothermal alteration: a case study of Dongping gold deposit Hebei Province, China. Chin J Geochem 22:45–57. https://doi.org/10.1007/BF02831545

Zhou ZX (1986) The origin of intrusive mass in Fengshandong, Hubei province. Acta Petrol Sin 2:59–70